



HAL
open science

Local hydrodynamic investigation by PIV and CFD within a Dynamic filtration unit under laminar flow

Xiaomin Xie, Claude Le Men, Nicolas Dietrich, Philippe Schmitz, Luc Fillaudeau

► To cite this version:

Xiaomin Xie, Claude Le Men, Nicolas Dietrich, Philippe Schmitz, Luc Fillaudeau. Local hydrodynamic investigation by PIV and CFD within a Dynamic filtration unit under laminar flow. *Separation and Purification Technology*, 2018, 198, pp.38-51. 10.1016/j.seppur.2017.04.009 . hal-01886464

HAL Id: hal-01886464

<https://hal.science/hal-01886464>

Submitted on 9 Jul 2021

HAL is a multi-disciplinary open access archive for the deposit and dissemination of scientific research documents, whether they are published or not. The documents may come from teaching and research institutions in France or abroad, or from public or private research centers.

L'archive ouverte pluridisciplinaire **HAL**, est destinée au dépôt et à la diffusion de documents scientifiques de niveau recherche, publiés ou non, émanant des établissements d'enseignement et de recherche français ou étrangers, des laboratoires publics ou privés.

1 **Local Hydrodynamic Investigation by PIV and CFD within a Dynamic**

2 **Filtration Unit under Laminar Flow**

3 Xiaomin XIE, Claude LE MEN, Nicolas DIETRICH, Philippe SCHMITZ, Luc FILLAUDEAU

4 LISBP, Université de Toulouse, CNRS, INRA, INSA, Toulouse, France

5

6 *Corresponding Author: Xiaomin XIE

7 Email: xxie@insa-toulouse.fr

8

9

10

11 Table of Contents

12	ABSTRACT.....	4
13	KEYWORDS.....	4
14	1 Introduction	5
15	2 Material and methods.....	9
16	2.1 Experimental setup.....	9
17	2.1.1 Circulation loop	11
18	2.1.2 PIV setup.....	11
19	2.1.3 PIV Data Acquisition and Processing.....	13
20	2.2 Test fluid and operating conditions.....	15
21	2.3 Statistical analysis for PIV	17
22	2.4 Flow field analysis with CFD	19
23	2.4.1 Governing equations and boundary conditions	19
24	2.4.2 Numerical method and calculation mesh.....	21
25	3 Results and discussions	22
26	3.1 From PIV measurement to velocity field analyses	22
27	3.2 Validation and analysis of CFD simulation.....	27
28	3.2.1 Simulated velocity fields.....	27
29	3.2.2 Vertical velocity and shear rate profile	29
30	3.2.3 Streamlines and RTD	33
31	3.3 Identification of the core velocity coefficient	35
32	4 Conclusions	36
33	Nomenclature:	38
34	Acknowledgement:	41
35	List of caption:.....	41
36	List of table:.....	42
37	Supplementary information:	42

38	Reference:.....	45
39		
40		

41 **ABSTRACT**

42 Local hydrodynamics within a complex and confined dynamic filtration module named
43 RVF (Rotating and Vibrating Filtration) was scrutinized under laminar flow with viscous
44 Newtonian fluid. This module was designed to treat complex fluids such as fermentation broth or
45 liquid food. Previous results reported global hydrodynamics (friction and power consumption
46 curves) and RVF efficiency during filtration of fermentation broths. However, the access to local
47 variables (shear rate, velocity) appeared as challenging in a confined volume. By associating
48 Particle Image Velocimetry (PIV) and an optical trigger strategy, the instantaneous velocity
49 fields were measured and analyzed. PIV experiments were carried out at 6 different planes in the
50 3 mm narrow gap between the membrane and the impeller, considering two feeding flowrates
51 ($Q_f=25$ and 45 L/h) under mixing rates 2 Hz. In addition, a simulation approach by
52 Computational Fluid Dynamics (CFD) was developed, confronted to PIV ($Q_f=45$ L/h, $N=2$ Hz)
53 and compared to global parameters.

54 In this work, we showed the ability to measure local velocity in a complex, confined and
55 rotating device. As expected, velocity in filtration cell was observed to be independent of
56 flowrate. Magnitude of mean velocity fluctuation was quantified and discussed as a function of
57 radial and axial position (constant impeller position). Moreover, velocity and shear rate profiles
58 were introduced by simulation, they proved that simulations were in a good agreement with PIV
59 measurements, and streamlines was also discussed combining Residence Time Distribution
60 (RTD). Finally, local and global core velocity coefficients (issued from PIV and CFD), as an
61 indicator of mechanical efficiency were calculated and compared to similar devices and
62 alternative methodologies which were reported in the literature.

63 **KEYWORDS**

64

65 **1 Introduction**

66 The principle of dynamic filtration (DF) is to generate complex hydrodynamic perturbations
67 (intensity, time dependent) by mechanical movement (rotation, vibration, oscillation) of
68 membrane or external mechanical forces close to the membrane, to better control membrane
69 fouling.

70 In the recent decades, many efforts and a great number of those studies have been done to
71 develop novel DF module and hydrodynamic study, in lab scale or pilot scale. Reviewing the
72 existing DF modules by our best of knowledge, they can be mainly classified by ‘*mobile*
73 *membrane*’ and ‘*stationary membrane + dynamic device*’ in terms of membrane motion, the
74 external force applied to the system can be longitudinal, transverse, torsional, or with a mix of
75 these motions. Early in the 1967, Sherwood et al. [1] suggested a rotating cylinder filter in
76 reverse osmosis for salt and water transport. Taking advantage from Taylor-Couette Flow in the
77 annulus with a relatively low rotation speed, cells and macromolecules can avoid being
78 destroyed. So this filter type was quickly applied to Pharmacy and Biological process such as
79 *Biodruck-filter* (BDF-01, Sulzer AG, Winterthur, Switzerland)[2], *Biopurification System* [3],
80 *RDF filter* (Rotary Dynamic Filtration) [4]. Lee. S et al. and Park et al.[5-7] also gave further
81 studies with the similar systems. Rotating disk membrane module such as *Rotating Membrane*
82 *Disk Filters (RMDFs)* [8], *Compact Rotating Disk (CRD filter)* [9], and *High shear rotary*
83 *membrane system (HSR-MS)* [10] are typical modules equipped with one or more rotating disk
84 membrane, other system like *Multi-shaft disk module (MSD, Westfalia Separator, Aalen,*
85 *Germany)*, stacks of membrane disks were driven by two or more shafts rotate in the same
86 direction, expected to have higher shear rate[11]. Similar rotating systems but installed with a

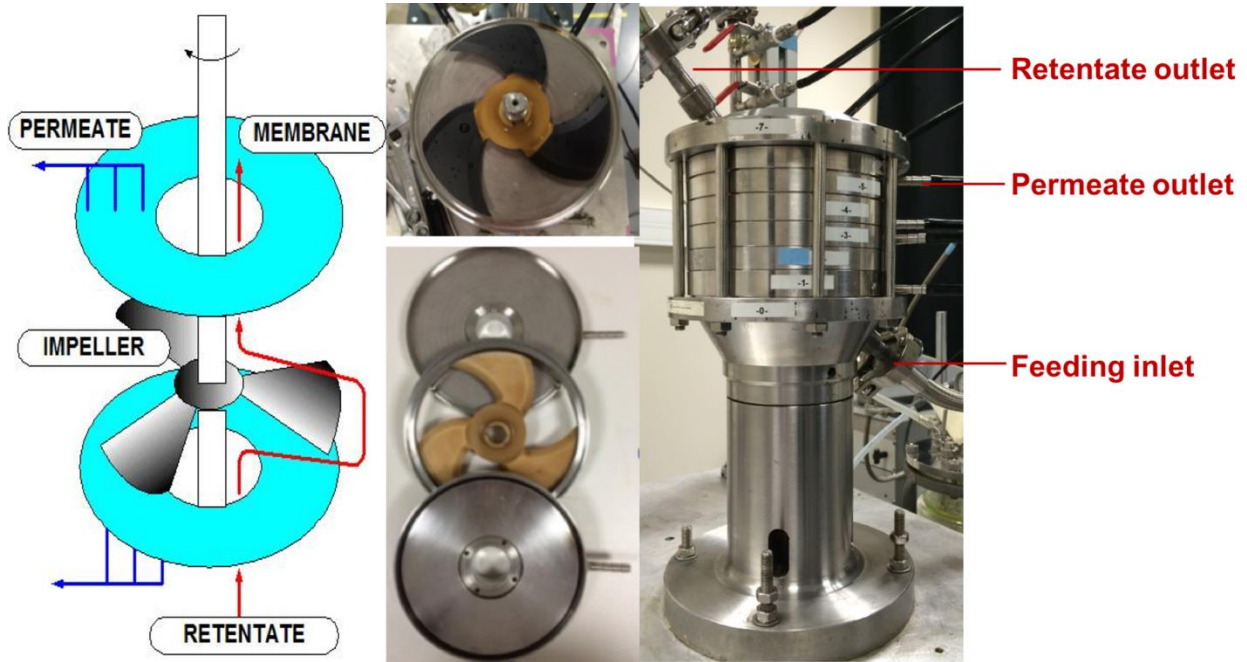
87 stationary membrane and a rotor close to it, were also widely studied. Main differences can be
88 found in rotor configuration, for example, *Dynamic Membrane Filter (DMF, Pall Corp.,*
89 *Cortland, NY)* [12-14] and *RDM (Rotating Disk Module)* [15,16] have a rotating disk, *Cross*
90 *Rotational Filters (CR-filters, Metso-Paper corp. Finland, ex: Raisio-Flootek, Finland, and ABB*
91 *Flootek, Sweden)* [17] was designed with a two-blade impeller, the *DYNO (Bokela GmbH,*
92 *Karlsruhe, Germany)* [18] and the *FMX (BKT United, Korea)* [19] filter installed with special
93 rotors to promote turbulence. Vibrating disk membrane module well known as *Vibratory Shear*
94 *Enhance Processing (VSEP, New Logic, USA) module* [20] and *Vibrating Membrane Filtration*
95 *module (PallSep-VMF)* [21], consists of overlapping membranes or membrane-coated disks in
96 series, mounted on a torsion bar driven by a motor transversely. Other popular module like
97 vibrating hollow fiber membrane filter are well documented in the literature as well [22,23]. All
98 these efforts contribute to high level of filtration quality, and enhanced efficiency. Compare with
99 dead-end filtration (DE) and cross-flow (CF) filtration, DF filtration has been proved better (1)
100 intensify filtration process and bioprocess, increase permeability and have higher biological
101 productivity by achieving high cell concentration, (2) reduce environmental impact (low loop
102 volume), (3) and reduce energetic consumption (uncoupling between retentate flowrate and wall
103 shear rate, working under low transmembrane pressure, TMP).

104 Enhancements in DF filtration is considered mainly come from the complex hydrodynamics
105 near the membrane surface, commonly known that the hydrodynamic flow field affects the
106 particle-liquid distribution and mass transfer of the membrane filtration process. Global
107 performances such as permeability, TMP, mean shear rate, fluid viscosity and power
108 consumption were well studied, however, less concern was reported in local variables. To have
109 access to local investigation, our attention was gravitated toward the field of visualization

110 measurement. One of the popular technique which has been widely used in this field is Particle
111 Image velocimetry (PIV), this technique can provide the local velocity distribution (or vector
112 map) by tracking the particle displacement in a given time interval. In DF filtration domain, PIV
113 measurement has been first applied in rotating cylindrical filters, Wereley et al. [24-26] gave a
114 detail of particles path and streamline spaced in different dimension and geometrical profile, help
115 to explain the physical fouling mechanism due to the cylindrical Couette flow and the Taylor
116 vortex flow. Figueredo-Cardero et al. [27] examined the flow field with in a thin gap between
117 inner and outer cylinder, mainly focus on the radial behavior. Other PIV measurement also
118 conducted with a rotating cone filter [28], a rotating flat-sheet (wing-like) membrane bioreactor
119 [29,30], a vibrating hollow fiber filter [31], a folded plate membrane module[32] to better
120 explain their filter performances by flow motion.

121 In this work, a local measurement using PIV technique had been carried out with an
122 innovative DF device, called Rotating and Vibrating Filtration (RVF technology – patent no. FR-
123 97-14825, RVF-filtration company, France). It consists of two identical filtration cells (Fig. 1a
124 shows one filtration cell) in series (4 membranes in total, filtration area 0.048 m^2 , volume 0.2 L
125 per cell, 1.5 L in total). And in each cell, as Fig. 1b shown, a three-blade impeller (flat blade,
126 diameter = 138 mm, thickness = 8mm) is driven by a central shaft continuously rotating (up to
127 50 Hz) in a 14mm gap between two porous substrate plates (membrane support in metal) which
128 drains the permeate, it gives a 3 mm gap between the impeller and the membrane surface.
129 Feeding fluid flows into the system from the inlet at the bottom, and go through the filtration
130 cells along the central shaft, then retentate flow out of the system from the outlet at the top.

131 This simple mechanical device runs continuously and generates a high shear rate as well as
132 a hydrodynamic perturbation in the small gap TMP (up to 300 kPa) and rotation frequency can
133 be adjusted to optimize the operating condition.



134
135

Fig. 1 Configuration of RVF module.

136 RVF module had been studied in previous papers [33-35]. In global point of view,
137 Qualitative and quantitative performances with different membrane material (hydrophilic and
138 hydrophobic properties), feeding fluid (water, clarified beer and rough beer, wine and crude
139 wine) and operating conditions (feeding flowrate, rotation speed, TMP, volume reduction factor)
140 have been reported. These papers proved that, RVF module could significantly intensify
141 filtration process and increase permeability gain. In fact, both global (power consumption,
142 pressure drop, heat dissipation, tracing) and local (radial pressure distribution at membrane
143 surface, velocity fields) hydrodynamic approaches were necessary to gain insights into the
144 complex hydrodynamic fields in the RVF and subsequently explain the better performances of
145 Membrane Bioreactor (MBR). Global hydrodynamic analysis indicates that the local variables

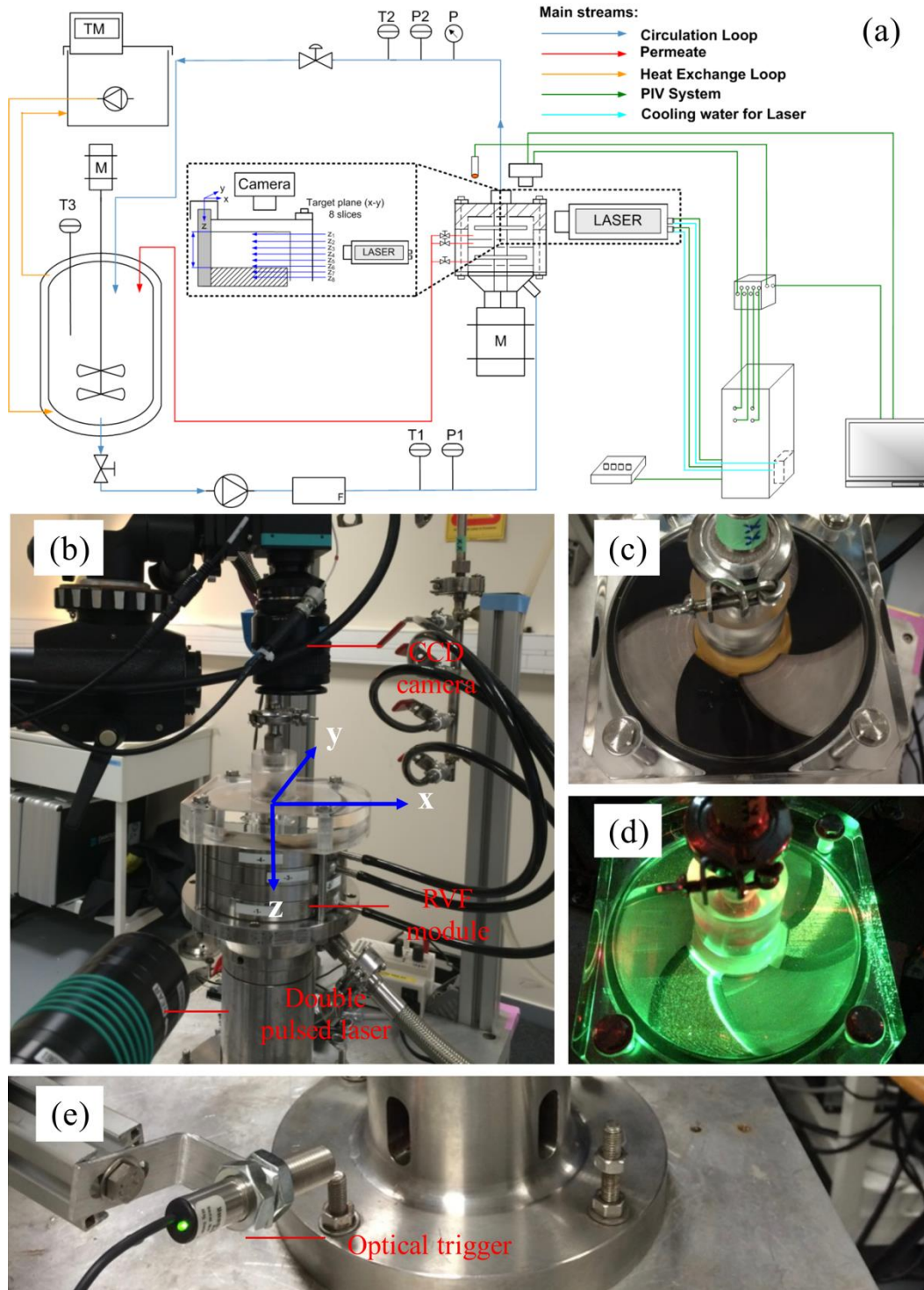
146 (shear rate, velocity and pressure) could not be easily estimated in the RVF module, the scientific
147 and technical challenge are inherent to the complex geometry of device (narrow gap, physical
148 enhancement for perturbation, etc.) and the rheological flow behavior (potential fluid like
149 multiphase fluid, high viscosity fluid, non-Newtonian etc.).

150 In this study, PIV experiments were performed within the RVF module in laminar flow
151 regime with a viscous Newtonian fluid, at 6 different planes in the 3 mm gap between the
152 membrane and the impeller (plus 2 additional planes in the gap between two impeller blades). In
153 parallel, numerical simulations were performed to have access to more parameters in flow
154 pattern. Our objective was to study and highlight the local hydrodynamics in a complex
155 configuration (narrow gap with complex shape of flat impeller), to better realize the consequence
156 of complex hydrodynamics on filtration and bioprocess performances, and also to give new
157 additional information (both in experiment and simulation) for filtering viscous fluid while it is
158 well known that high viscosity fluid is not easy to be filtered.

159 **2 Material and methods**

160 2.1 Experimental setup

161 A fully instrumented circulation loop combined with PIV system was developed for
162 experimental measurement.



163

164 Fig. 2 Schematic diagram and apparatus used in the experiment (a) F: flowmeter; P1/P2: pressure

165 sensor of inlet/outlet; T1/T2/T3: temperature sensor of inlet/outlet/bioreactor; P: pressure gauge;

166 TM: Thermostat; (b) The PIV system synchronized with a CCD camera, double pulsed laser and

167 the RVF module with the transparent cell; (c-d) black-painted impeller in the transparent cell; (e)
168 An optical trigger synchronized with PIV system

169 2.1.1 Circulation loop

170 As the schematic Fig. 2 (a) shows, RVF module is integrated in a fully instrumented closed
171 circulation loop: outlet and bypass of the RVF module are linked back to the feeding tank. In this
172 loop, the feeding flow is pumped from a double-jacket feeding tank (2 L), which is connected
173 with a thermostat to maintain a constant temperature. Flowrate is controlled by a volumetric
174 pump (Head: TUTHILL CO., series A54739, Drive: GROSCHOFF CO., series PM8014,
175 3800rpm, DC motor control unit: DART 250G series) and measured by a flow meter (Altometer
176 IFM 1080/6). Temperature and pressure are measured by thermal sensor (PT100) and pressure
177 gauge (Endress Hauser Cerabar S PMC 731, $0-4 \times 10^3$ kPa), installed both at the inlet and outlet
178 respectively. A third thermal sensor is fixed in the feeding tank. Power consumption of RVF
179 module is calculated by measurement of current (Ammeter, LEM Co. AC current transducer AT-
180 B10) and tension (Voltmeter, SINEAX U 504 31 LD). All the sensors are connected to a digital
181 data acquisition system (AGILENT 34972A LXI) and convert to numerical data record by a PC.

182 2.1.2 PIV setup

183 Besides, as it displays in Fig. 2 (a) and (b), RVF module is also integrated with the PIV
184 system which has traditional elements. In this study, measurements were focused at the
185 horizontal plane (x - y plane). Due to the complex configuration of RVF, velocity field in vertical
186 plane (y - z or x - z plane) was difficult to be obtained, this work will be included in the future. PIV
187 system was supported and maintained by DANTEC DYNAMICS Co. (Denmark), basic elements
188 are required as Fig. 2 (b) shown:

- 189 • The stainless steel filtration cell is replaced by a transparent cell as shown in (b);

- 190 • A fluorescent dye called Rhodamine B (powder) was used in this experiment, it has
191 homogeneous distribution and good ability to present the flow motion and scatter the
192 light from laser beams in our test fluid. Pretreatment was conducted with sonication
193 (Elmasonic S 60 H, 50/60 Hz) for dissolving of particles in liquid, particle size
194 ranged from 10 to 20 μm . Particle settling kinetics was carried out by TurbiscanLab
195 (Fomulation) with test fluid and has no significant decantation;
- 196 • A flat light source (pulsed laser, Model: LISTRON NANO L200-15 PIV, max
197 trigger frequency 15 Hz) to illuminate the target plane and the florescent particles;
- 198 • A CCD (Charge Coupled Device) camera (DANTEC Dynamic, Flow sense EO,
199 $2048 \times 2048 \text{ px}^2$, pixel size $7.4 \mu\text{m}$, max frequency 15 Hz) should focus on the target
200 plane (perpendicular to the flat laser sheet);
- 201 • A processor and timer box is needed to communicate with the camera and the pulsed
202 laser.
- 203 • Importantly, an optical trigger, as it shown in Fig. 2 (e), is also connected to the
204 timer box. In this case, acquisition signal was sent by this trigger when it detected a
205 marker on the shaft (which drives the impeller), images were always taken with the
206 same impeller position.
- 207 • Moreover, it was assumed that no impact of permeate flux on the local velocity
208 distribution, due to its low quantity compare with the feeding flow, thus permeate
209 loop was closed and no membrane was used.

210 By using all the material and strategy above, the flat laser sheet beamed on the target area
211 (x - y plane) between the upper wall (of the filtration cell) and the impeller surface, and could be
212 adjusted to 6 slices as Fig. 2 (a) shown (step by 0.5 mm in z direction from the wall to the

213 impeller, $z_1=0.25$ mm, $z_2=0.75$ mm, $z_3=1.25$ mm, $z_4=1.75$ mm, $z_5=2.25$ mm, $z_6=2.75$ mm, with
214 uncertainty ± 0.25 mm according to the thickness of laser sheet). Two additional slices were
215 scrutinized at $z_7= 4.75$ mm and $z_8= 6.75$ mm in order to access to velocity fields between two
216 blades. Since Rhodamine tracers were used in this case, a red filter is placed in front of the
217 camera to allow only fluorescent light (reflected from particles) enter the camera, while
218 reflection of the transparent cell is filtered out.

219 2.1.3 PIV Data Acquisition and Processing

220 The PIV measurement was performed in a field of 109×109 mm² view, focus on one third of
221 the filtration cell in x - y (horizontal) plane, this area was capturing one leading edge and one
222 trailing edge. Flow field was assumed to be periodic since it was agitated by a 3-blades impeller.
223 This 1/3 area was considered to represent the whole filtration cell. The raw image processing was
224 evaluated by using commercial software DynamicStudio.2015a (by DANTEC DYNAMIC,
225 Denmark). A statistical adaptive cross-relation algorithm was used to find average particles
226 displacement with a mask input to filter the non-interested area, and iteratively adjust and
227 determine an appropriate Interrogation Area (IA) size and shape (specified criteria is needed) to
228 local seeding density and flow gradient. An adaptive IA window was used to start with 32×32
229 px² to 16×16 px² window for the calculation, corresponding to 1.70×1.70 mm² and 0.85×0.85
230 mm², a 50% window overlapping was also applied to improve correlation. Therefore, each
231 velocity map has theoretically 128×128 vectors, with about 9000 valid and 7389 disabled by the
232 mask, while approximately 1% bad vectors had been rejected. The time interval between two
233 images in each pair was controlled between 500-800 μ sec according to different operating
234 conditions, it only allowed the particle displacement move approximately a quarter of the
235 window size. Other parameters can be found in Tab. 1.

Parameters	Setting
Image size	2048×2048px ²
Interrogation window	adaptive PIV from 16×16 px ² to 32×32 px ² , step size 16×16 px ²
Particle density	5-10 particles per interrogation window (16px ×16px)
Particle size	Mean diameter of 10-20 μm
Calibration	Scale factor : 7.177 ; 1 pixel= 7.177×7.4=53 μm
Time interval between consecutive images, Δt	500-800 μsec
Frequency of acquiring/ trigger rate	Synchronized with impeller rotation speed
Number of samples	1000 of image pairs

237 Performed adaptive PIV processing, data was subsequently applied to MATLAB software
 238 (developed by MathWork) through a code for further analysis. Velocity profile at the given
 239 radius was calculated by Inverse Distance Weighting Interpolation (IDW) as the following
 240 equation:

$$U_m(x, y) = \frac{\sum_{j=1}^n [U_m(x_j, y_j) \cdot w_j]}{\sum_{j=1}^n w_j}, \quad \text{with } w_j = \frac{1}{h_j^p} \quad (1)$$

241 Where w_j is a weight factor assigned by the distances h_j between the reference points
 242 (value-known) and the interpolation point (value-unknown). $U_m(x, y)$ is the interpolation point
 243 and $U_m(x_j, y_j)$ is the neighbor vector as a reference input, n is the number of reference vectors
 244 and we put 4 in this case, p is an exponent value (power index, default value 2), determines how
 245 quickly the influence of neighboring points drops off, the higher value the closer vector influence
 246 more.

247 By this method, velocity profiles at any given radius and layer in the gap can be reported.
 248 It has to be highlighted that acquisition frequency was kept by the optical trigger and that the
 249 main purpose of this article was to study the flow field and velocity profile in different
 250 component.

251 2.2 Test fluid and operating conditions

252 A water soluble and viscous transparent Newtonian fluid (Breox® Polyalkylene Glycol 75
 253 W 55000, BASF) was used. The thermo-physical properties including viscosity μ [Pa·s], density
 254 ρ [kg/m³], heat capacity C_p [J/(kg·°C)] versus temperature T [°C] and mass concentration C [%]
 255 were respectively measured with a rheometer (HAAKE Mars III, SN: 4201100100779, Thermo
 256 Scientific, Germany, torque range: $10^{-8} - 0.2$ N·m, rotation speed range: $10^{-7} - 4500$ RPM), a
 257 density meter (DE40, SN: MPK38384, Mettler Toledo, France, range: 10^{-4} to 3 g/cm³ $\pm 10^{-4}$
 258 g/cm³, 4 to $90^\circ\text{C} \pm 0.05^\circ\text{C}$), and a differential scanning calorimeter (Micro DSC-III, SN:
 259 60/50287.06.102, Setaram, France, temperature range: $-20 - +120^\circ\text{C}$, thermal kinetics: $10^{-3} -$
 260 $+1.2^\circ\text{C}$ and fluxmeter range: $0.2 \mu\text{W} - 20$ mW, resolution : 40nW). Density, viscosity and heat
 261 capacity are described as functions of Breox® mass concentration and temperature ($15 - 45^\circ\text{C}$)
 262 as follows:

$$\begin{cases} Cp = aT + b \\ a = -14.8C^2 + 16.3C - 1.46 (R^2 = 0.974) \\ b = -2.17 \times 10^3 C + 4.30 \times 10^3 (R^2 = 0.972) \end{cases} \quad (2)$$

$$\begin{cases} \rho = cT + d \\ c = 0.185C + 1.00 (R^2 = 0.999) \\ d = -9.74 \times 10^{-4} C - 2.58 \times 10^{-4} (R^2 = 0.999) \end{cases} \quad (3)$$

$$\begin{cases} \ln\mu = -\frac{Ea}{R} \left(\frac{1}{T} - \frac{1}{T_{20}} + \ln\mu_{20} \right) \\ Ea = -1.80 \times 10^4 C - 1.90 \times 10^4 (R^2 = 0.964) \\ \ln(\mu_{20}) = -7.88C^2 + 19.7C - 6.78 (R^2 = 0.999) \end{cases} \quad (4)$$

263 With these regression equations, fluid properties of BREOX solution can be easily estimated. A
 264 40% (mass concentration) diluted BREOX solution was chosen as a test fluid (with $\mu = 0.81$
 265 Pa·s, $C_p = 3274$ J/(kg·°C) and $\rho = 1067$ kg/m³ at $T=20^\circ\text{C}$). Temperature of the feeding tank was
 266 controlled at 20°C by adjusting the thermostat (room temperature was air controlled at 20°C).
 267 Rotation speed of the impeller (N) was fixed at 2 Hz, feeding flowrate (Q_f) controlled at 25 and
 268 45 L/h. Additionally, during these measurements, the fluid properties and operating parameters
 269 were stable (permanent regime).

270 According to the previous study [33], Reynolds and mixing Reynolds can be estimated:

$$Re_{mixing} = \frac{\rho N d_m^2}{\mu} = 45 \quad (5)$$

Laminar regime: $Re_{mixing} < 400$, turbulent regime: $Re_{mixing} > 1 \times 10^6$;

$$Re_Q = \frac{\rho u_f d_h}{\mu} = \frac{2\rho Q}{\mu \pi d_h} = 0.01 \quad (6)$$

Laminar regime: $Re_Q < 3$, turbulent regime: $Re_Q > 50$.

271 With d_m is the diameter of the impeller, d_h (equal to 3 mm) is the equivalent
 272 hydraulic diameter of the RVF module. Therefore, at $N=2$ Hz, laminar regime is
 273 confirmed.

- 274 • Temperatures at inlet and outlet of RVF module exhibit only 0.2°C increase.
 275 Considering thermal dependency of physical properties, the variation of viscosity,
 276 density and heat capacity can be neglected and a permanent regime is assumed;
- 277 • Pressure difference between inlet and outlet was 49.2 ± 2 kPa at 45 L/h corresponding
 278 to 0.63 W;
- 279 • Mixing power was measured at 33.5 ± 0.6 W for 2Hz.

280

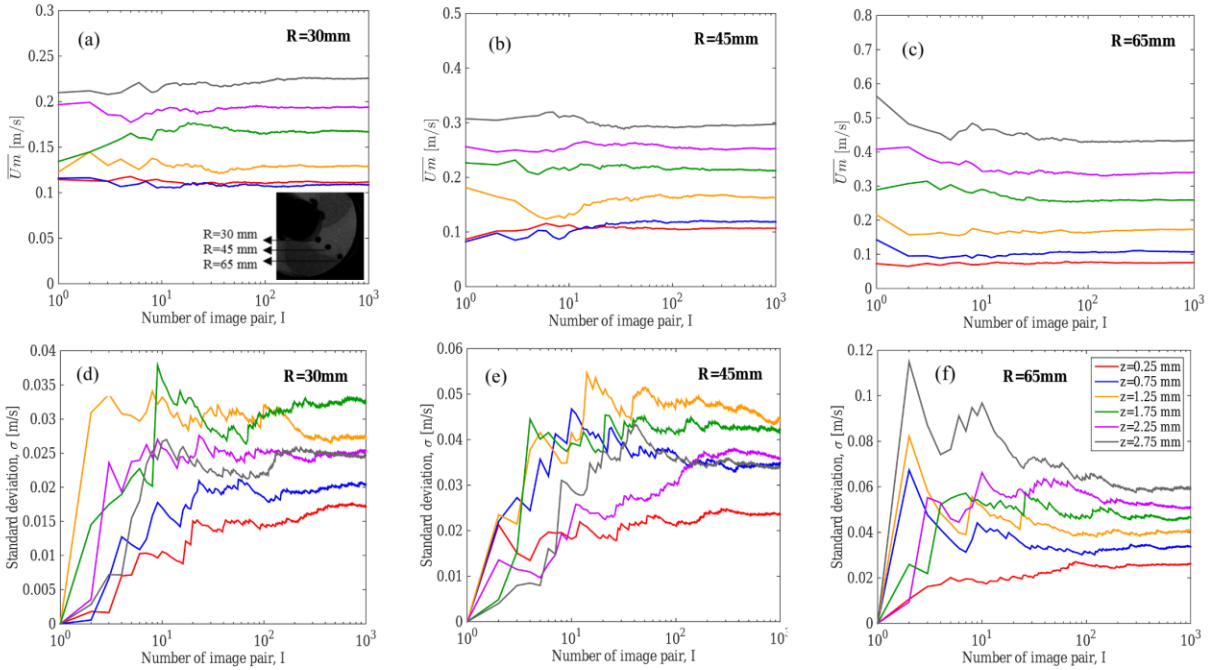
281 2.3 Statistical analysis for PIV

282 The amount of images on the flow statistics (mean values and standard deviation) was
283 investigated to determine and to optimize PIV measurements. The reliability and stability of
284 velocity fields were verified in order to access to the required number of image pairs. In Fig. 3,
285 the mean value of velocity magnitude $\overline{U_m}$ (Eq. 7) and the standard deviation σ_I (Eq. 8) are
286 calculated from velocity field in random points, and are plotted as a function of image number
287 (I).

$$\overline{U_{m_I}} = \frac{1}{I} \sum_{i=1}^I [U_{m_i}], \quad I = 1, 2, \dots, 1000. \quad (7)$$

$$\sigma_I = \sqrt{\frac{1}{I} \sum_{i=1}^I (U_{m_i} - \overline{U_{m_I}})^2}, \quad I = 1, 2, \dots, 1000. \quad (8)$$

288 $\overline{U_{m_I}}$, it is defined as an accumulative moving average as well as σ_I is defined as an
289 accumulative moving standard deviation,.



290

291 Fig. 3 Evolution of mean IDW velocity (a, b and c) and the associated standard deviation (d, e and f) as a
 292 function of the number of image pairs, I . Observations are reported for 3 radius (30, 45 and 65 mm) for 6
 293 different slices within the gap ($z_j=0.25$ to $z_6=2.75$ mm) at $\theta=-50^\circ$.

294

From Fig 3a, b and c, an increase of mean velocity from the wall to the impeller (gap
 295 position) is observed whatever radius for position $\theta=-50^\circ$. Fig 3d, e and f indicate a large
 296 variation of standard deviation magnitude without correlation with gap position. For example, at
 297 $R=45$ mm for $z_j=0.25$, $z_3=1.75$ and $z_6=2.75$ mm, $\overline{U_{m100}}$ values are respectively 0.1, 0.25 and 0.3
 298 m/s whereas σ_{100} values are respectively 0.02, 0,04 and 0,035. Graphically, $\overline{U_{mI}}$ and σ_I seems to
 299 converge to stable and constant values for $I >50$ and $I >100$ respectively. Some studies argued
 300 that large number of frames was needed, especially for turbulent flow characterization.
 301 Figueredo-Cardero et al. [27] proposed that 4000 image pairs had to be used, T. Li et al.[31] used
 302 a total of 300 image pairs for fouling investigation in a hollow fiber setup, while T.Jiang et al.[36]
 303 and N.Liu et al.[37] used only a small amount around 50 image pairs for their analysis, while

304 larger number of image pairs are required in other research fields like aeronautics and
 305 aerodynamics [38,39]. In our conditions, convergence criterion, $\left|\frac{d\overline{u_{mI}}}{dI}\right|$ and $\left|\frac{d\sigma_I}{dI}\right|$ are defined. A
 306 constant decreasing slope of $\log\left(\frac{d\overline{u_{mI}}}{dI}\right)$ and $\log\left(\frac{d\sigma_I}{dI}\right)$ vs $\log(I)$ is noticeable and absolute
 307 criterion, $<10^{-4}$, are used to estimate the minimum requested number of image pairs. For $\overline{U_{mI}}$ and
 308 σ_I , I superior to 200 is identified and $I=1000$ was retained, although it is overestimated.

309 2.4 Flow field analysis with CFD

310 To simulate numerically the flow field in this dynamic filtration module, a model based on
 311 the finite element method was developed using commercial CFD software COMSOL.
 312 Multiphysics (version 4.3a, U.S).

313 2.4.1 Governing equations and boundary conditions

314 The geometrical domain was simplified to one filtration cell of RVF module. Assuming a
 315 periodic movement of the impeller, one third of the filtration cell is simulated and the governing
 316 equations are solved in a rotating reference frame. Considering a laminar and incompressible
 317 flow of a Newtonian fluid, mass and momentum balances were governed by the Navier Stokes
 318 equations expressed in a fixed reference frame as follows:

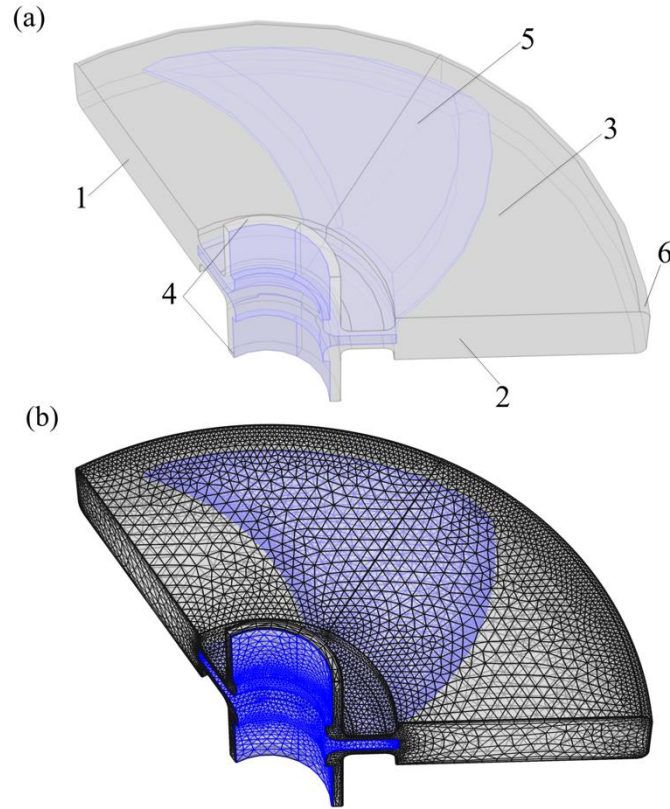
$$\nabla \mathbf{u} = 0 \quad (9)$$

$$\rho \cdot \frac{\partial \mathbf{u}}{\partial t} + \rho(\mathbf{u} \cdot \nabla \mathbf{u}) = -\nabla p + \mu \nabla^2 \mathbf{u} \quad (10)$$

319 where ρ is the fluid density in kg/m^3 , μ is the fluid dynamic viscosity in $\text{Pa}\cdot\text{s}$, P is the pressure in
 320 Pa, and \mathbf{u} is the absolute velocity vector in m/s .

321 Navier Stokes equations were solved under boundary conditions related to fluid domain,
 322 wall and impeller which describe real working conditions:

- 323
- Simulation focused on one third of the filtration cell and flow fields were assumed to
324 be periodic at $\theta = 0^\circ$ and 120° (Fig. 4 (a), section 1 and 2);
 - A mean pressure gradient, as the driving force, was imposed to the entire volume of
325 the filtration cell across the whole length from the bottom to the top (Fig. 4 (a),
326 section 4);
 - On the impeller surface (Fig. 4 (a), surface 5), radial velocity vector u_r and vertical
328 velocity vector u_z were imposed to 0, angular velocity vector $u_\theta = 2\pi NR$, was
329 expressed from rotation frequency of the impeller, with N, the rotation frequency
330 [Hz] and R, radial coordinate [m];
 - Velocity vectors on all the walls, including membrane surfaces (upper and lower
332 wall) and the surrounding wall (Fig. 4 (a), surfaces 3 and 6) were imposed to 0
333 considering no-slip boundary conditions at fluid-solid interface;
334



335
 336 Fig. 4 Geometry of the RVF filtration cell (a) and mesh (b) used with CFD software COMSOL 4.3a. For
 337 fluid, sections 1 and 2: vertical periodic cross sections and section 4: fluid inlet (bottom) and outlet (top)
 338 sections. For impeller, surface 5: rotating solid impeller. For wall, surfaces 3 and 6: horizontal membrane
 339 surfaces including upper and lower walls and surrounding wall.

340 2.4.2 Numerical method and calculation mesh

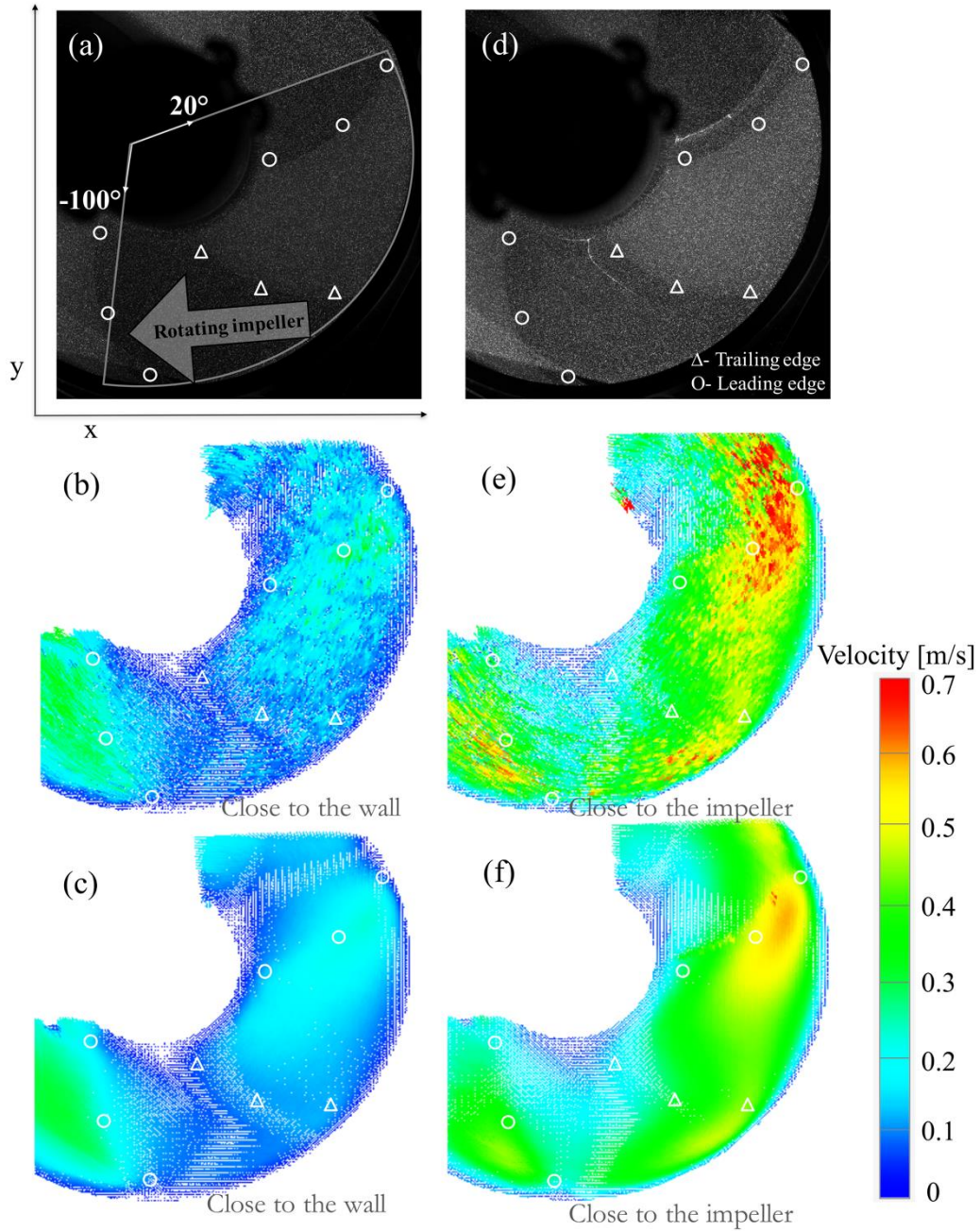
341 Eq. (9) and (10) were solved by the Rotating Machinery Model of COMSOL 4.3a, which
 342 was a time-dependent 3D problem. Selected mesh was a compromise between accuracy and
 343 reduction of the calculation time. For the simulations dealing purely with laminar flow, a physics
 344 controlled and refined mesh (automatically generated by COMSOL 4.3a) was chosen (Fig. 4b).
 345 Several element types were used, such as tetrahedral, pyramid, prism, triangular, quadrilateral,
 346 edge and vertex elements, with total number of 355362, total volume 55 mL. Large velocity
 347 gradient was carefully considered with local refined mesh.

348 For CFD simulation, a Newtonian fluid with a viscosity equal to 0.8 Pa·s was considered
349 and assumed to be incompressible and independent of temperature in agreement with test fluid
350 for PIV measurements. Simulated conditions were rotation frequencies equal to 2, 5 and 10 Hz,
351 vertical mean pressure gradients, $\frac{(P_{inlet}-P_{outlet})}{L}$, equal to 1.17, 1.10 and 1.02 Pa/m corresponding
352 to nominal flowrate equal to 45 L/h. One additional simulation was realized for Q=25 L/h, 2 Hz
353 and a vertical mean pressure gradients equal to 0.76 Pa/m.

354 **3 Results and discussions**

355 3.1 From PIV measurement to velocity field analyses

356 By analyzing the PIV raw images, the instantaneous velocity fields (from single images
357 pair) and time averaged mean velocity fields (from 1000 image pairs) in 6 horizontal plane (x - y
358 plane) within membrane-impeller gap were computed. To acquire the mean velocity fields in this
359 rotating system, the optical trigger plays a key role in these measurements because it
360 synchronizes and governs the laser generator and the camera with the position of one specific
361 blade. Image processing and statistical quantities ($\overline{U_m}$, σ_I) were detailed in Materials & Methods
362 then velocity components in the angular and radial directions were calculated. Velocity fields
363 (Fig. 5) and profiles (Fig. 6) are presented and compared to the CFD simulation (Fig 7 and 8).



364

365

366

367

368

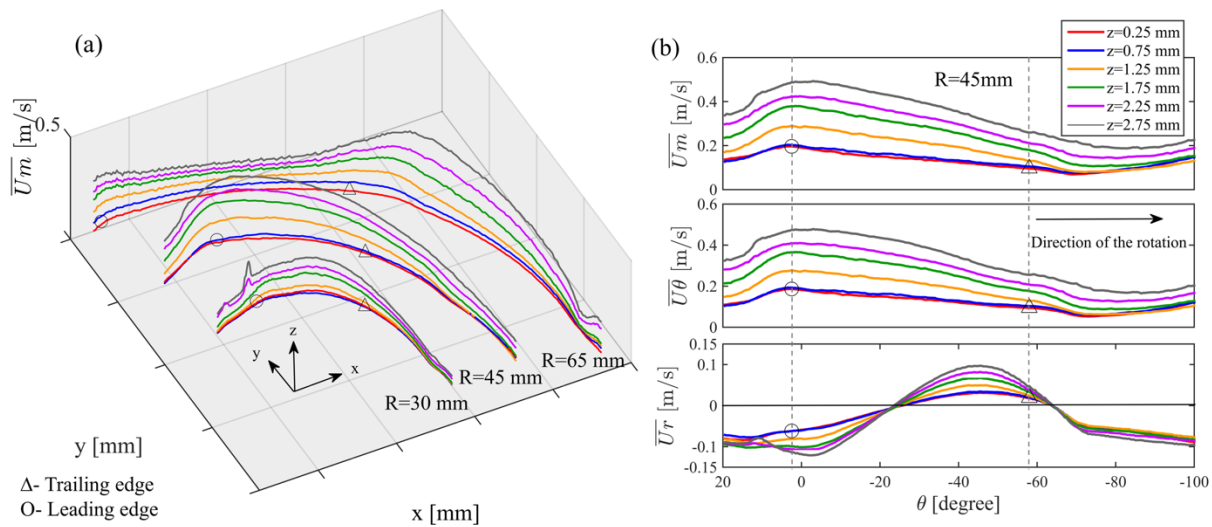
369

Fig. 5 Illustration of PIV raw images (a, d), instantaneous velocity fields (b, e, issued from single image pair) and time-averaged velocity fields (c, f, averaged of 1000 image pairs) in RVF module. Slice positions: close to the wall, $z_1=0.25\text{mm}$ (a, b and c) and close to the impeller, $z_6=2.75\text{ mm}$ (d, e and f); Operating conditions: $Q_f= 45\text{ L/h}$, $N=2\text{ Hz}$; $\mu=0.81\text{ Pa}\cdot\text{s}$ and $T=20^\circ\text{C}$. Symbols: O, leading edge and Δ , trailing edge of blade.

370 Fig. 5 provides an overview of the magnitude of velocity fields. In our experimental
371 conditions, maximal impeller velocity is equal to 0.87 m/s at $R=69$ mm ($d_m=138$ mm). Raw PIV
372 images, Fig 5a and d show the constant position of impeller and the homogeneous surface
373 density of florescent particles for $z_1=0.25$ (close to membrane) and $z_6=2.75$ (close to impeller)
374 mm. In terms of flow pattern, instantaneous (Fig 5b and e) and mean (Fig 5c and f) velocity
375 fields can be compared. As it stands, Fig 5b and c present the lowest velocity magnitudes
376 whereas Fig5e and f exhibit the highest values (close to the impeller velocity). As expected,
377 mean velocity fields present a uniform and regular flow pattern. Jiang.T et al.[36,40] also
378 introduced a PIV measurement by using pine pollen tracing in water (turbulent flow) with a
379 rotating membrane bioreactor. This membrane module was consisted of 9 identical flat sheets
380 vertically in a cylindrical reactor, with internal diameter of 240 mm and effective volume of 13
381 L. In their conditions, mean velocity fields show a clear and stable velocity gradient in radial
382 direction with time-averaged velocity plot. In our study, similar observation can be established:

- 383 • It is found that velocity around the central shaft is regular and organized, and it is
384 close to zero. As it described in Introduction part, feeding fluid goes through RVF
385 module along the central shaft vertically (z direction) from the bottom to the top,
386 governing velocity vector is at the z direction, so, velocity close to the central shaft
387 in horizontal (x - y) plane is almost zero;
- 388 • Velocity gradient increases in radial direction from inner to outer diameters, but
389 velocity remains nearly equal to zero at the maximum diameter $R=70$ mm (fluid is at
390 rest close to the surrounding wall, no-slip boundary conditions at fluid-solid
391 interface). This observation is verified for both position, $z_1=0.25$ and $z_6=2.75$ mm;

- 392 • Velocity magnitude close to the inner diameter, $R=25\text{mm}$, remains inferior to 0.1
- 393 m/s whereas shaft velocity is equal to 0.31 m/s;
- 394 • Velocity fields likely have periodic movements generated by the specific shape of
- 395 impeller. Maximum fluid velocities (Fig 5c and f) were found near the leading edge
- 396 of the blade. At $R=65\text{ mm}$, the maximum values were 0.15 and 0.45 m/s for $z_I=0.25$
- 397 and $z_6=2.75\text{ mm}$ respectively, while the impeller velocity was 0.82 m/s. However,
- 398 maximum value in the velocity field $z_I=0.25\text{ mm}$ and $z_6=2.75\text{ mm}$ are at $R=55\text{-}60\text{ mm}$,
- 399 with 0.21 and 0.58 respectively;



400

401 Fig. 6 Evolution of mean velocity profiles, \overline{U}_m and their radial and angular components, $\overline{U}_\theta, \overline{U}_r$ as a

402 function of angular position for 6 horizontal planes (z) within the membrane-impeller gap. (a):

403 interpolated mean velocity at $R= 30, 45$ and 65 mm ; (b): mean, radial and angular velocity profiles,

404 $\overline{U}_m, \overline{U}_\theta$ and \overline{U}_r , at $R=45\text{ mm}$. Operating conditions: $Q_f= 45\text{ L/h}$, $N=2\text{ Hz}$; $\mu=0.81\text{ Pa}\cdot\text{s}$ and $T=20^\circ\text{C}$.

405 Symbols: \circ , leading edge and \triangle , trailing edge of blade.

406 From velocity fields, several velocity profiles can be more specifically analyzed. Fig. 6a

407 presents the evolution of IDW mean velocity magnitude \overline{U}_m profiles at 3 given radius (30, 45

408 and 65 mm) for 6 axial positions ($z_I= 0.25$ to $z_6=2.75\text{ mm}$). From this overview, However, the

409 unexpected velocity peaks (about 0.35 m/s) which locate at $R=30$ mm $z_6=2.75$ mm can be
410 pointed out as they have the same magnitude as impeller velocity (0.38 m/s). An artifact most
411 likely caused by the fluorescent particles accumulated on the blade edge is assumed and PIV
412 system considers those particles in data treatment.

413 In Fig 6b, mean velocity profiles versus angular position ($-120^\circ < \theta < +10^\circ$) in one third of
414 filtration cell are presented at $R=45$ mm within a reconstructed polar coordinate centered at the
415 middle of RVF shaft. Both components were derived from the Cartesian velocity by
416 decomposing the velocity vector into radial and tangential components, $\overline{U_m^2} = \overline{U_\theta^2} + \overline{U_r^2}$.
417 Profiles were observed to be periodic and sustain previous observation with velocity fields. As
418 expected, maximum velocity in RVF occurs close to the impeller ($z_6=2.75$ mm), and decrease
419 gradually from the impeller to the wall without any disruption between the layers. It indicated
420 that laminar flow within the gap was highly stable and well-organized. In addition, some
421 noticeable waves appear around the leading edge and trailing edge (symbol O and Δ), probably
422 due to the shape of three blades. It might imply that this impeller design could periodically
423 generate a regular fluctuation along the angular direction, and tended to remove the membrane
424 fouling even with highly viscous fluids. Specific remarks can be summarized from Fig. 6b:

- 425 • $\overline{U_m}$ and $\overline{U_\theta}$ are statistically similar. Since RVF module is an annulus mixing device
426 with an impeller equipped with three flat blades, the dominant velocity component is
427 $\overline{U_\theta}$.
- 428 • $\overline{U_r}$ has a negligible contribution in value but fluctuates with a highly organized ebbs
429 and flows, probably due to the impeller design.
- 430 • Besides, velocity profiles were also compared with two feed flowrates (25 and 45
431 L/h). Results showed that no significant impact on velocity profiles was observed. It

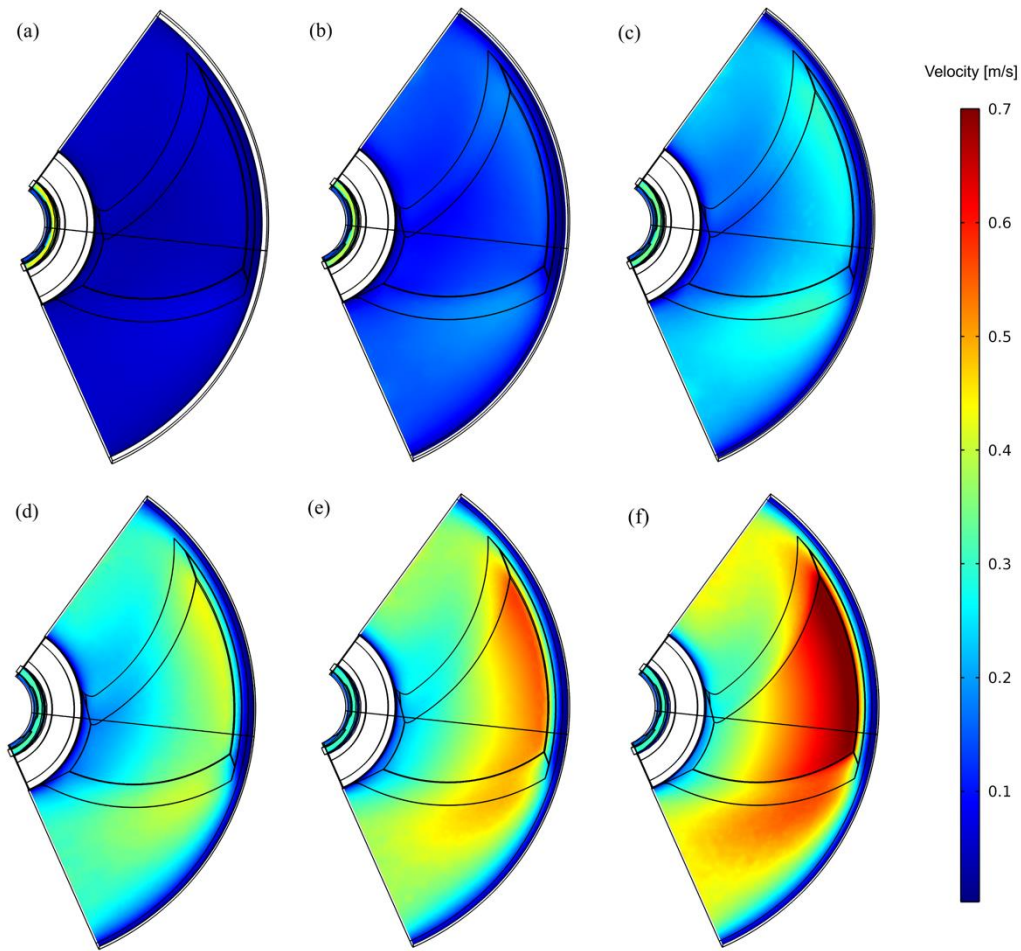
432 corroborated one of the advantages of DF compare to the conventional filtration
433 (DE, CF) with an internal flow pattern independent from feed flowrate.

434 3.2 Validation and analysis of CFD simulation

435 CFD simulation is a powerful tool to estimate and get access to the additional information
436 in a flow field when experiment is hardly possible to perform. Therefore, in this second step, PIV
437 experiments and CFD simulations ($\mu=0.81$ Pa·s, $Q_f=45$ L/h, $N=2$ Hz, $T=20$ °C) were compared to
438 validate simulation model, and then to gain insight into local hydrodynamics.

439 3.2.1 Simulated velocity fields

440 CFD give access to velocity in x , y and z coordinate, results present in this part is velocity
441 magnitude in the x - y plane associated with PIV measurements.



442

443 Fig. 7 Simulated velocity fields in 6 slices (a-f): z_1 to $z_6=2.75$ mm. Operating conditions: $Q_f=45$ L/h, $N=2$
 444 Hz; $\mu=0.81$ Pa·s and $T=20^\circ\text{C}$.

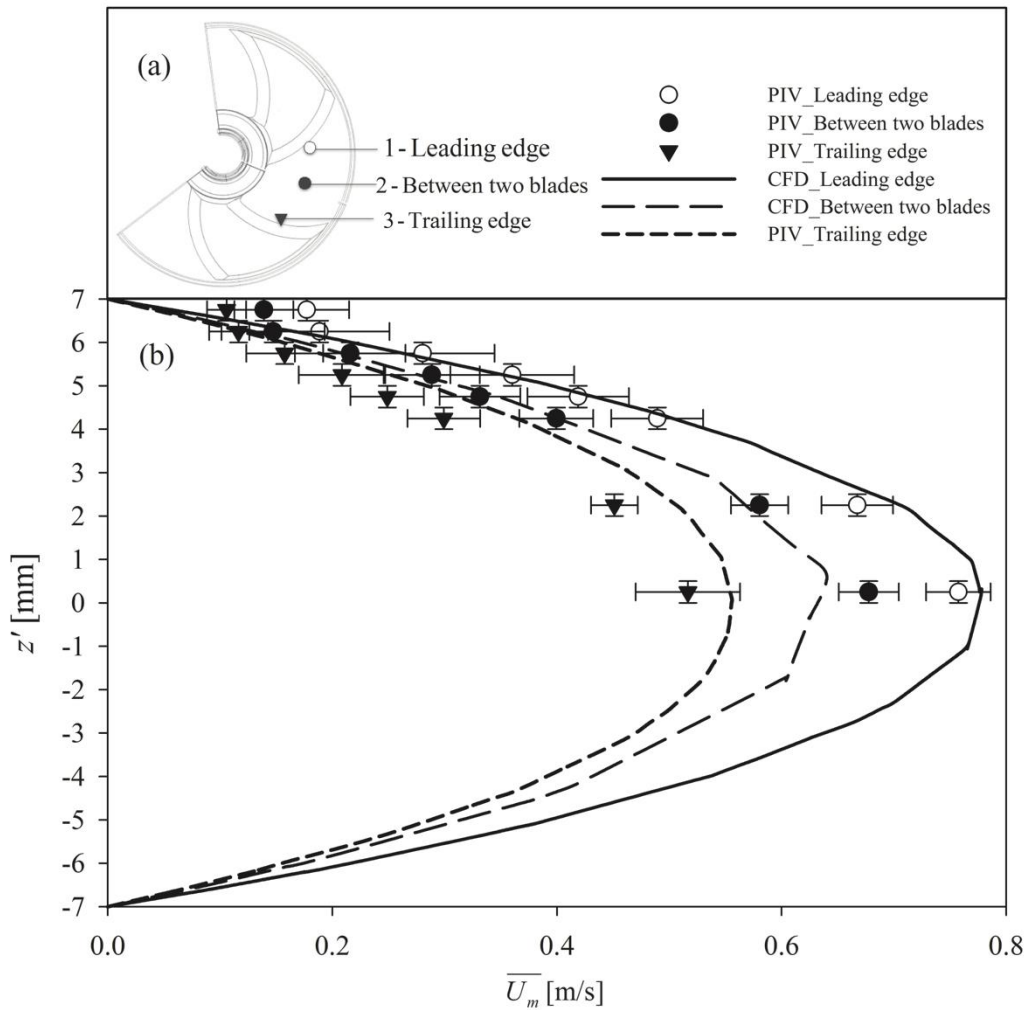
445 In Fig. 7 (a), velocity fields at 6 slices are plotted to appreciate velocity magnitude and
 446 deviation. A first qualitative approach (Fig. 5 and Fig. 7) is aim to compare the simulated and
 447 experimental velocity fields :

- 448 • Velocities are nearly equal to zero when the flow layers are close to the wall (z_1),
 449 while the closest to the impeller present the highest values (z_6);
- 450 • Velocity is nearly zero close to the central shaft and the surrounding wall ($R=70$
 451 mm) of the filtration cell;

- 452 • Maximum velocities occur at leading edge at $R=55-60$ mm of the impeller for (a)
453 (b) (c) and (d) which has been found also in Fig. 5, but for (e) and (f), it is found
454 above the blade body;
- 455 • Differences between PIV and CFD may come from the precision and uncertainty of
456 measurement, as we described, adjusting the measuring plane may have ± 0.25 mm
457 error due to the laser thickness.

458 3.2.2 Vertical velocity and shear rate profile

459 As mentioned, PIV measurements were performed in half of the filtration cell from z_1 to z_8 .
460 Due to optical obstruction of laser beam, velocity field in z_7 and z_8 can only measure between 2
461 blades and provided very limited information, while CFD simulations were applied to the entire
462 filtration cell (within 14 mm gap $-7 < z' < 7$ between both membranes, impeller thickness $-4 < z' < 4$).

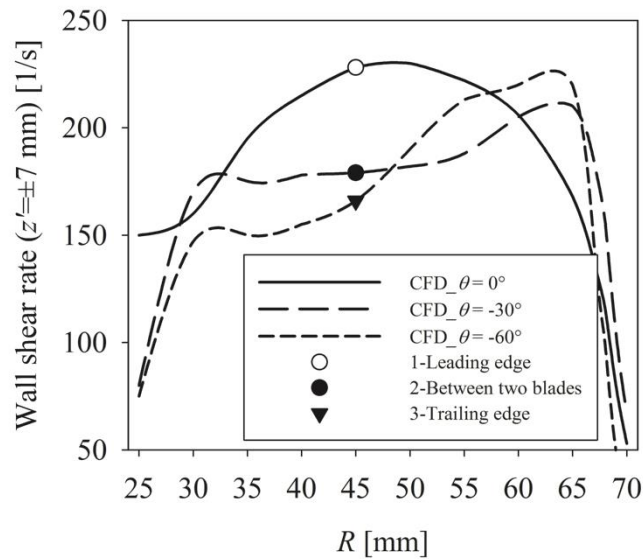


463

464 Fig. 8 Evolution of mean velocity, \overline{U}_m issued from PIV measurement and CFD simulations as a function
 465 of axial direction, z' for 3 points located between 2 blades at radius, $R=45$ mm (point 1: leading edge,
 466 point 2: between two blades, point 3: trailing edge). Operating conditions: $Q_f=45$ L/h, $N=2$ Hz; $\mu=0.81$
 467 Pa·s and $T=20^\circ\text{C}$. (Notice: $z'=-z+7$ is used, lead to: $-7 < z' < 7$ for the 14 mm gap between both walls where
 468 membranes are mounted, $-4 < z' < 4$ for the impeller thickness)

469 Fig. 8 compares velocity profiles at radius $R=45$ mm between PIV measurements and CFD
 470 simulation. All curves issued from CFD simulations present a typical parabolic laminar profile
 471 between two fixed walls for point 1 (leading edge at $\theta=0^\circ$), 2 (between two blades at $\theta=-30^\circ$) and
 472 3 (trailing edge at $\theta=-60^\circ$). Between 2 blades, the maximum velocities were located at the

473 parabolic vertex corresponding to the middle of filtration cell ($z'=0$ mm). Between blade and
474 membrane, the maximum velocity can be observed at blade surface (Fig. 6b). Velocity at leading
475 edge (Point 1) is higher than the two others (point 2 and 3) with a maximum velocity of
476 0.757 ± 0.029 m/s in PIV and 0.778 m/s in CFD. For points 2 and 3, maximum velocities were
477 respectively 0.678 ± 0.027 m/s and 0.517 ± 0.046 m/s for PIV and 0.641 m/s and 0.556 m/s for
478 CFD. However, theoretical angular velocity of the impeller is 0.56 m/s at $R=45$ mm, a tentative
479 inference on this result is that special configuration (narrow gap, confined volume with rotating
480 three-blade impeller) have great influence in local velocity field and thus has complex
481 hydrodynamic in the filtration cell, according to author's limited knowledge. Regarding
482 maximum velocities, the consistency between PIV and CFD is well established. Considering
483 whole velocity profiles, the same trends could be observed even if the profile at trailing edge is
484 slightly overestimated with CFD. Slight deviations are justified by uncertainty of experimental
485 measurements regarding laser sheet location and velocity.



486

487 Fig. 9 Wall shear rate ($z'=\pm 7$ mm) calculated from CFD simulations with 3 points from radius $R=25$ to 70
 488 mm. Operating conditions: $Q_f=45$ L/h, $N=2$ Hz; $\mu=0.81$ Pa·s and $T=20^\circ\text{C}$. (Notice: $z'=\pm 7$ mm is at the
 489 surface of the walls where membranes are mounted)

490

491

492

493

494

495

496

497

498

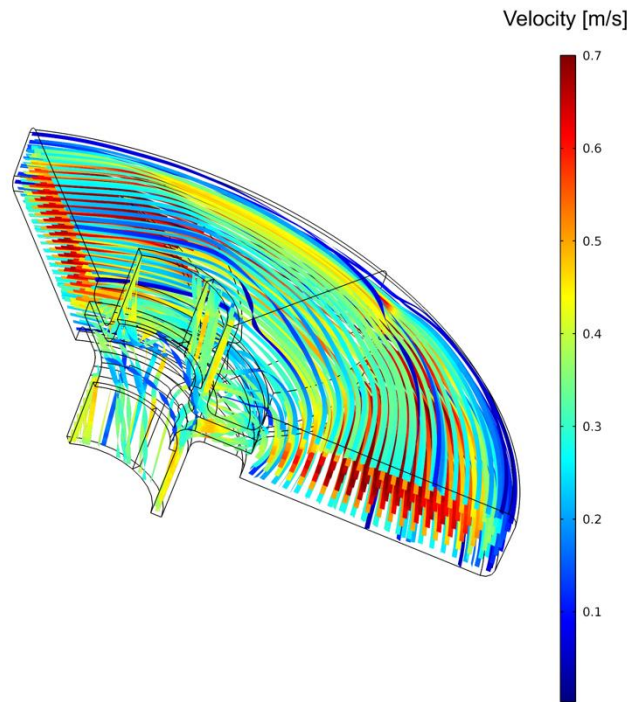
499

Velocity magnitudes and parabolic shapes sustain the accurate fitting between PIV and CFD, local shear rate can be estimated from CFD to introduce the hydrodynamic phenomena in the filtration cell. To this end, wall shear rate profiles at 3 angular position are plotted in Fig. 9 (shear rate profile are symmetrical at $z'=\pm 7$ mm, absolute values are almost the same). In our operating conditions ($Q_f=45$ L/h, $N=2$ Hz; $\mu=0.81$ Pa·s and $T=20^\circ\text{C}$), wall shear rate are equal to 229, 179 and 164 1/s for points 1, 2 and 3 respectively at radius $R=45$ mm. At this radius, it was found that wall shear rate at leading edge is higher than the others. Wall shear rate profile for $\theta=0^\circ$ increases from 150 1/s ($R=25$ mm) up to 230 1/s ($R=50$ mm) then decreases to 50 1/s at the surrounding wall ($R=70$ mm). Profiles at $\theta=-30^\circ$ and $\theta=-60^\circ$ are having a similar trend, both increase from 75 1/s ($R=25$ mm) and have a rapid decrease at $R=65$ mm. This information may

500 indicate a complex hydrodynamics at the membrane surface, and it is also intensified by the
501 complex shape of impeller and its rotation.

502 3.2.3 Streamlines and RTD

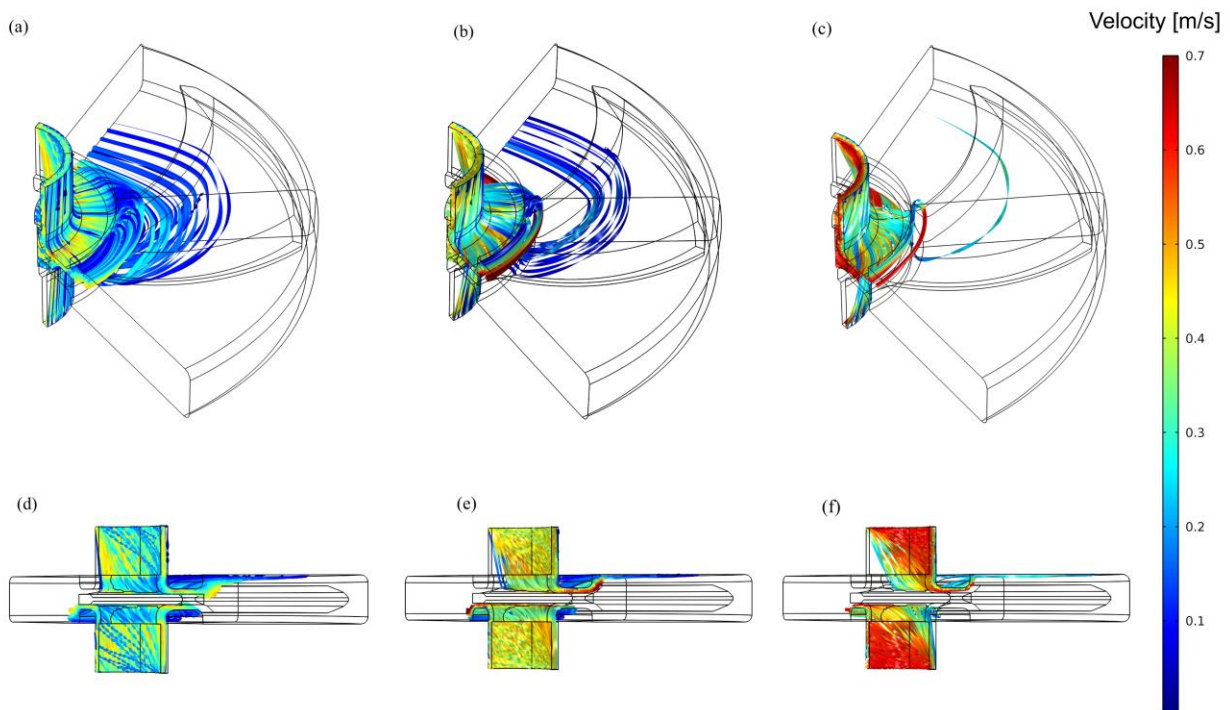
503 So far, investigation of hydrodynamics in RVF module have occurred at different scales,
504 ranging from filter efficiency at a global experiment point of view (in previous studies) up to
505 local examination of velocity field (in this study). To complete this hydrodynamic, it requires the
506 information of fluid residence time and the track of mixing, it fills the blank of information
507 regarding how long the microbial cell can survive from such a complex filter, and also realize the
508 mixing effect. Comparison between PIV experiments and CFD simulations has proved
509 simulation approach was validated in laminar flow, which proved the access to additional flow
510 patterns information is feasible, whereas experimental approaches is hardly possible. Therefore,
511 in present case we pay attention to streamlines issued from CFD in order to access and discuss
512 Residence Time Distribution (RTD) and the mixing effect within the RVF filtration cell.



513

514 Fig. 10 Illustration of streamlines in the filtration cell issued from CFD simulation, introduce streamlines
 515 in horizontal slices at 2 Hz with in the whole filtration cell. Operating conditions: $Q_f= 45 \text{ L/h}$; $\mu=0.81 \text{ Pa.s}$
 516 and $T=20^\circ\text{C}$.

517 Fig. 10 display the streamlines within the filtration cell between section 1 and 2 in Fig.4.
 518 The streamlines seem to be almost parallel to each other, indicating a well-organized flow
 519 motion in any horizontal plane around the shaft. As expected Streamlines velocity is found
 520 almost equal to zero close to the surrounding wall, it highly refers to an annular surrounding
 521 volume with low mixing, and a dead-zone can be assumed. However, a large magnitude of
 522 velocity between the streamlines is noticeable, velocity value corresponds to the velocity field in
 523 Fig. 7.



524
 525 Fig. 11 Illustration of streamlines in the filtration cell issued from CFD simulation in 3D (a, b, c) and 2D
 526 (d, e, f) view, introduces the streamlines from inlet to outlet (Fig. 4, section 4), at rotation frequency $N=2$

527 Hz (a, d), $N=5$ Hz (b, e), $N=10$ Hz (c, f). Operating conditions: $Q_f=45$ L/h; $\mu=0.81$ Pa.s and $T=20^\circ\text{C}$. *

528 Notice each figure has 500 streamlines.

529 In addition, Fig 11 presents the streamlines corresponding to inlet and outlet section (Fig 4,
530 section 4).CFD simulations were conducted in order to investigate the effect of mixing rate, to
531 realize the contribution of the impeller to RTD in the system. It is clear that shortcut effect along
532 the shaft is a dominant phenomenon. Graphically, from (a) to (c) with the increase of rotation
533 speed, less streamlines pass over the entire filtration cell although each figure has 500
534 streamlines. It seems the flow has a shortcut straight from the inlet to the outlet. And it is further
535 proved by the streamlines in the vertical view (d), (e) and (f): with the increase of rotation speed,
536 vertical streamlines have higher velocity, it means that fluid left the system faster in this zone.
537 And the flow in the rest of the cell hold steady and rotate in stable. To sum up, streamlines
538 confirm that a dominant shortcut flux may exist along the shaft, consequently less flux flow into
539 the filtration cell; the contribution of the shortcut in vertical direction became more prevalent
540 with the increase of rotation speed, it may cause a risk of dead-zone in the filtration cell.

541 3.3 Identification of the core velocity coefficient

542 Core velocity coefficient K_θ is one of the key factors that present the mechanical efficiency
543 of the RVF, to realize the device mechanical efficiency as an indicator. This coefficient can be
544 raised by increasing surface roughness and changing device configuration. Among the early
545 studies, Wilson et al.[41] found K_θ (ratio of fluid velocity to impeller velocity, $K_\theta = \frac{\langle \overline{U_\theta} \rangle}{\omega \cdot R}$) was
546 close to 0.313 between a stationary and a rotating disk with suction. Bouzerar et al.[42] increased
547 this coefficient up to 0.62 by modifying the rotating disk in a DF module via pressure
548 measurement, and further increased up to 0.84 by Brou. et al.[15]. For the complex designed
549 RVF module (three-blade and narrow-gap configuration), previous work [34] resulted a value of

550 0.71 by pressure measurement. However, these coefficients presented in the literature gave a
551 global ratio between the impeller and the turbulent core fluid layer. By our experiment, local K_θ
552 distribution can be identified. In the z direction, from the wall to the impeller, K_θ varies from
553 0.08 to 0.54 with a mean value of 0.31 in laminar flow, and slightly decreases from inner radius
554 to the outer radius, affected by the surrounding wall. This result was in a good agreement with
555 the simulation result which gives a mean value of 0.35.

556 **4 Conclusions**

557 Among the numerous filtration studies, including our past work, researchers developed a
558 lot of application by using DF, research mainly apply to low viscosity filtration and have dealt
559 with (a) fouling mechanisms, (b) the relationship between quantitative and qualitative
560 performances, (c) the development of alternative membrane filtration such as membrane
561 structure and dynamic filtration and (d) industrial applications. It is demonstrated that dynamic
562 filtration can be an efficient substitute for some conventional filtration. Good performance has
563 been proved in food engineering process such as beer, dairy, juice etc., and also used in
564 biomedicine such as bovine serum albumin and cell harvest, as well as in drinking
565 water/wastewater treatment plant, and fermentation industry. Less attention has been paid in the
566 local flow field. Therefore, we suggested that, our earlier result of global hydrodynamic analysis
567 should be strengthened by the determination of local variables (shear rate, velocity and pressure)
568 which cannot be easily estimated in a confined volume, the RVF module. We have, however,
569 obtained the access to the local hydrodynamics associated with high viscosity fluid, by using
570 PIV, a powerful flow-visualization technique.

571 In this paper, PIV measurements were done in 6 horizontal planes (8 planes in Fig. 8) with
572 an optical trigger, we show the ability to access to local velocity fields in a complex, confined

573 and rotating device by PIV technique, and compared to simulation. Firstly, results issued from
574 PIV were discussed, such as velocity field and velocity profile in radial and vertical direction,
575 and it had been proved that local velocity profile were highly organized and steady, moreover, it
576 was independent of feeding flowrate. Furthermore, CFD simulation was performed in parallel,
577 presented a good agreement with PIV measurements, enabled us to validate the numerical model
578 and have the ability to estimate some more local variables precisely. Finally, local and global
579 core velocity coefficients (issued from PIV and CFD) were deduced and compared to similar
580 devices and alternative methodologies reported in the literature. These results lead to conclude
581 that:

- 582 • velocity distribution in such a filter was strongly affected by complex physical
583 configuration (three blades and narrow gap), it helped to generate a complex but
584 periodic velocity variation;
- 585 • we believed that RVF may have high efficiency in fouling removal, since it had
586 high wall shear rate even with very viscous fluid in pure laminar flow, and also
587 proved by the high value of velocity coefficient;
- 588 • Less power would be consumed by RVF module compared to traditional filtration
589 type, since it had been proved that velocity in the filtration cell was independent of
590 feeding flowrate, high pressure of feeding pump was released;
- 591 • CFD model was validated, it can be used to scrutinized micro-hydrodynamics in
592 the RVF module;

593 Overall, this work highlighted the local hydrodynamic phenomena in a DF module, and it
594 was motivated by the lack of information in local aspect of this filter, to better understand the
595 physical mechanism as an extended support for those good performances in the past work.

596 However, we had not discussed on the vortex that may possible occurred. It should be notice that
 597 flow in the filtration device is a three-dimension phenomenon. Due to the technical limitation
 598 like complexity of experimental setup and limitation of author’s knowledge, the current study
 599 was only focus on two-dimension measurement, which was parallel to the flat impeller surface.
 600 Further studies may include PIV measurement in vertical plane, then it will be interesting for the
 601 velocity decomposition by Proper Orthogonal Decomposition (POD) analysis in both horizontal
 602 and vertical plane to further identify the flow pattern and velocity structure. More research on
 603 RTD is also required to validate simulated streamline in this article, it is important to realize in
 604 such dramatic hydrodynamics when work with biological fluid.

605 **Nomenclature:**

Latin Letter		
C_p	Specific heat capacity	[J/(kg·°C)]
d_h	$d_h = \frac{4S}{P}$, Equivalent diameter (P is the wetted perimeter)	[m]
d_m	Diameter of the impeller	[m]
h_i	Distance from reference points to the interpolation point	[mm]
I	Number of image pair	[/]
K_θ	Core velocity coefficient	[/]
n	Number of the reference points	[/]
N	Rotation frequency of the impeller	[Hz]
r	Radial coordinate	[mm]
R	Radius	[mm]
p	Power index	[/]

P_{in}	Inlet pressure	[Pa]
P_{out}	Outlet pressure	[Pa]
Q_f	Feeding flowrate	[L/h]
Re_{mixing}	$Re_{mixing} = \frac{\rho N d_m^2}{\mu}$, Reynolds number for a mixing system	[/]
Re_Q	$Re_Q = \frac{\rho u_f d_h}{\mu}$, Reynolds number for a system equivalent to a tube	[/]
T	Temperature	[°C]
TMP	Transmembrane Pressure	[Pa]
\overline{U}_m	Magnitude of the velocity vector	[m/s]
\overline{U}_θ	Velocity of the vector at tangential direction	[m/s]
\overline{U}_r	Velocity of the vector at radial direction	[m/s]
w_i	Weight factor	[/]
x-y plane	Horizontal plane parallel to the impeller surface	[/]
x	x coordinate	[mm]
y	y coordinate	[mm]
z	z coordinate	[mm]
Greek symbol		
μ	Viscosity	[Pa·s]
ρ	Density	[kg/m]
ω	Angular velocity of the impeller	[rad/s]

θ	Angle, centered at the middle of the rotating shaft	[degree]
σ_I	Accumulative moving standard deviation of velocity magnitude, I stands for numbers of image pairs	[m/s]
Δ_t	Time interval between two image for one image pair	[μ s]
Other Symbol		
Δ	Trailing edge of the impeller	[/]
O	Leading edge of the impeller	[/]
Abbreviation		
CF	Cross-flow	
CFD	Computational Fluid Dynamic	
DF	Dynamic Filtration	
DE	Dead-end (filtration)	
IA	Interrogation Area	
IDW	Inverse Distance Weighting interpolation	
MBR	Membrane Bioreactor	
PIV	Particle Image Velocimetry	
RVF	Rotating and Vibrating Filtration module	

607 **Acknowledgement:**

608 Financial support by China Scholarship Council is gratefully acknowledged (grant No.
609 201304490066). Authors wish to thank José Moreau and Bernard REBOUL (LISBP) for their
610 mechanical contribution and Pascal DEBREYNE (PIHM, Lille) for data acquisition and
611 electrical control for experimental setup.

612 **List of caption:**

613 Fig. 1 Configuration of RVF module.

614 Fig. 2 Schematic diagram and apparatus used in the experiment (a) F: flowmeter; P1/P2: pressure
615 sensor of inlet/outlet; T1/T2/T3: temperature sensor of inlet/outlet/bioreactor; P: pressure
616 gauge; TM: Thermostat; (b) The PIV system synchronized with a CCD camera, double
617 pulsed laser and the RVF module with the transparent cell; (c-d) black-painted impeller in
618 the transparent cell; (e) An optical trigger synchronized with PIV system

619 Fig. 3 Evolution of mean IDW velocity (a, b and c) and the associated standard deviation (d, e
620 and f) as a function of the number of image pairs, I . Observations are reported for 3 radius
621 (30, 45 and 65 mm) for 6 different slices within the gap ($z_1=0.25$ to $z_6= 2.75$ mm) at $\theta=-50^\circ$.
622 .

623 Fig. 4 Geometry of the RVF filtration cell (a) and mesh (b) used with CFD software COMSOL
624 4.3a. For fluid, sections 1 and 2: vertical periodic cross sections and section 4: fluid inlet
625 (bottom) and outlet (top) sections. For impeller, surface 5: rotating solid impeller. For wall,
626 surfaces 3 and 6: horizontal membrane surfaces including upper and lower walls and
627 surrounding wall.

628 Fig. 5 Illustration of PIV raw images (a, d), instantaneous velocity fields (b, e, issued from single
629 image pair) and time-averaged velocity fields (c, f, averaged of 1000 image pairs) in RVF
630 module. Slice positions: close to the wall, $z_1=0.25$ mm (a, b and c) and close to the impeller,
631 $z_6=2.75$ mm (d, e and f); Operating conditions: $Q_f= 45$ L/h, $N=2$ Hz; $\mu=0.81$ Pa·s and
632 $T=20^\circ\text{C}$. Symbols: \circ , leading edge and \triangle , trailing edge of blade.

633 Fig. 6 Evolution of mean velocity profiles, U_m and their radial and angular components, U_θ , U_r
634 as a function of angular position for 6 horizontal planes (z) within the membrane-impeller

635 gap. (a): interpolated mean velocity at $R= 30, 45$ and 65 mm; (b): mean, radial and angular
636 velocity profiles, U_m, U_θ and U_r , at $R=45$ mm. Operating conditions: $Q_f= 45$ L/h, $N=2$ Hz;
637 $\mu=0.81$ Pa·s and $T=20^\circ\text{C}$. Symbols: \circ , leading edge and \triangle , trailing edge of blade.

638 Fig. 7 Simulated velocity fields in 6 slices (a-f): z_1 to $z_6=2.75$ mm. Operating conditions: $Q_f= 45$
639 L/h, $N=2$ Hz; $\mu=0.81$ Pa·s and $T=20^\circ\text{C}$.

640 Fig. 8 Evolution of mean velocity, U_m issued from PIV measurement and CFD simulations as a
641 function of axial direction, z' for 3 points located between 2 blades at radius, $R=45$ mm
642 (point 1: leading edge, point 2: between two blades, point 3: trailing edge). Operating
643 conditions: $Q_f= 45$ L/h, $N=2$ Hz; $\mu=0.81$ Pa·s and $T=20^\circ\text{C}$. (Notice: $z'=-z+7$ is used, lead to:
644 $-7 < z' < 7$ for the 14 mm gap between both walls where membranes are mounted, $-4 < z' < 4$ for
645 the impeller thickness)

646 Fig. 9 Wall shear rate ($z'=\pm 7$ mm) calculated from CFD simulations with 3 points from radius
647 $R=25$ to 70 mm. Operating conditions: $Q_f= 45$ L/h, $N=2$ Hz; $\mu=0.81$ Pa·s and $T=20^\circ\text{C}$.
648 (Notice: $z'=\pm 7$ mm is at the surface of the walls where membranes are mounted)

649 Fig. 10 Illustration of streamlines in the filtration cell issued from CFD simulation, introduce
650 streamlines in horizontal slices at 2 Hz with in the whole filtration cell. Operating
651 conditions: $Q_f= 45$ L/h; $\mu=0.81$ Pa·s and $T=20^\circ\text{C}$.

652 Fig. 11 Illustration of streamlines in the filtration cell issued from CFD simulation in 3D (a, b, c)
653 and 2D (d, e, f) view, introduces the streamlines from inlet to outlet (Fig. 4, section 4), at
654 rotation frequency $N=2$ Hz (a, d), $N=5$ Hz (b, e), $N=10$ Hz (c, f). Operating conditions: $Q_f=$
655 45 L/h; $\mu=0.81$ Pa·s and $T=20^\circ\text{C}$. * Notice each figure has 500 streamlines.

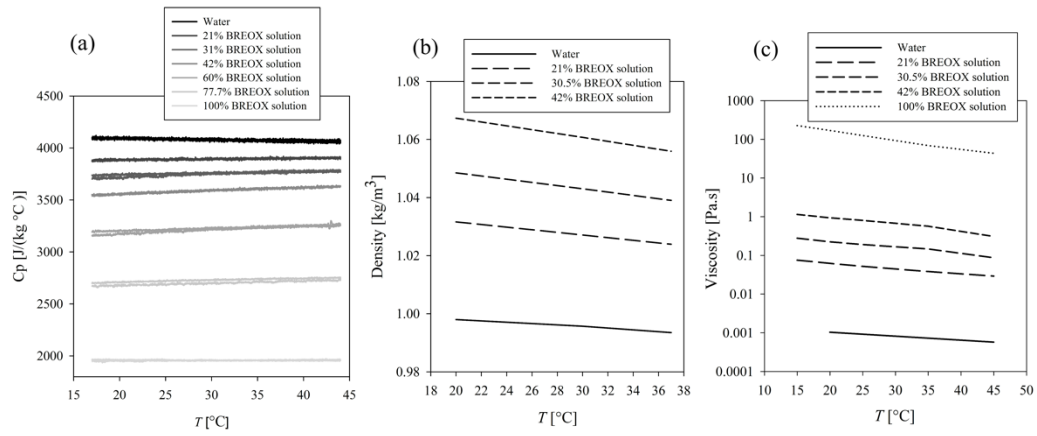
656

657 **List of table:**

658 Tab. 1 System acquisition parameters of PIV setup

659 **Supplementary information:**

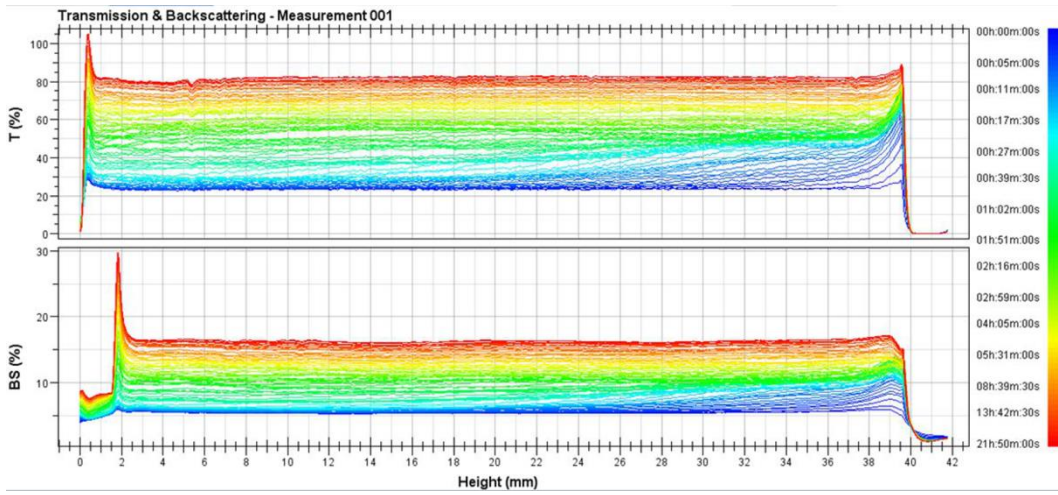
660 Properties of BREOX:



661

662

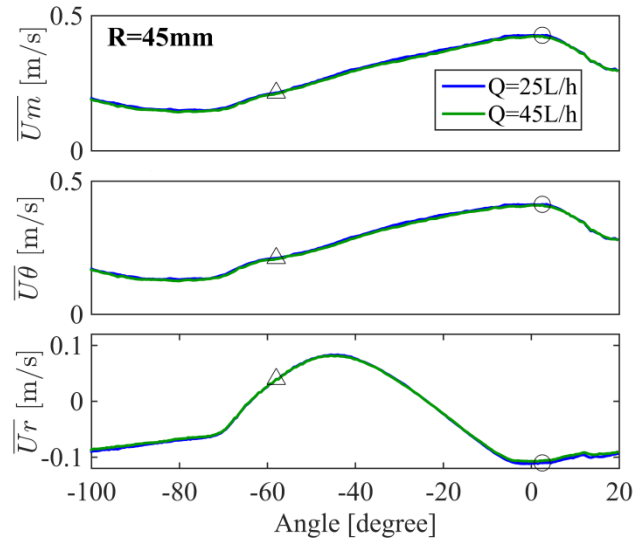
Fig. A.1



663

664

Fig. A.2



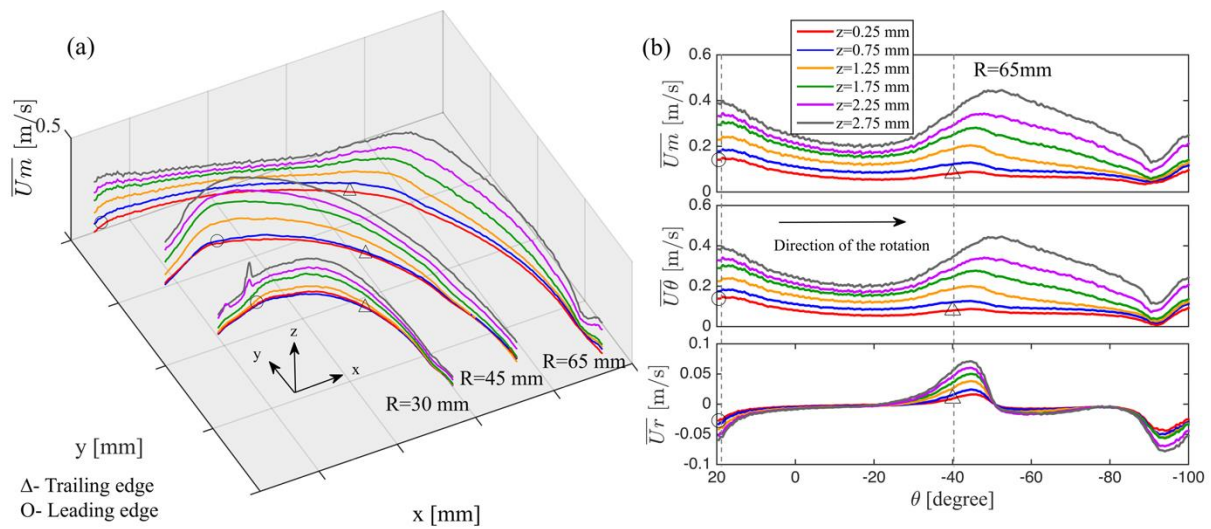
665

666

Fig. A.3 Comparison of velocity components with two flowrates (Measurement position: $R=45$ mm,
 $z=2.25$ mm)

667

668



669

670

Fig. A.4 Mean radial velocity profiles (\overline{U}_m) and their velocity components ($\overline{U}_\theta, \overline{U}_r$) for 6 horizontal

671

planes. (a) Overview of interpolated mean velocity magnitude profiles at $R= 30, 45$ and 65 mm, within

672

the gap by 6 slices ($Q_f= 45$ L/h, $N=2$ Hz); (b) Velocity profiles of \overline{U}_m , and their components $\overline{U}_\theta, \overline{U}_r$, at

673

65 mm radius.

674

676 **Reference:**

- 677 [1] T.K. Sherwood, P.L.T. Brian, R.E. Fisher, Desalination by Reverse Osmosis, *Ind.*
678 *Eng. Chem. Fund.* 6 (1967) 2–12. doi:10.1021/i160021a001.
- 679 [2] K.H. Kroner, V. Nissinen, Dynamic filtration of microbial suspensions using an
680 axially rotating filter, *Journal of Membrane Science.* 36 (1988) 85–100.
681 doi:10.1016/0376-7388(88)80009-7.
- 682 [3] M. MATEUS, J. CABRAL, Steroid Recovery by a Rotary Membrane System,
683 *Biotechnology Techniques.* 5 (1991) 43–48. doi:10.1007/BF00152754.
- 684 [4] A. Adach, S. Wroński, M. Buczkowski, W. Starosta, B. Sartowska, Mechanism of
685 microfiltration on the rotating track membrane, *Separation and Purification*
686 *Technology.* 26 (2002) 33–41. doi:10.1016/S1383-5866(01)00114-9.
- 687 [5] S. Lee, R.M. Lueptow, Experimental verification of a model for rotating reverse
688 osmosis, *Desalination.* 146 (2002) 353–359. doi:10.1016/S0011-9164(02)00512-X.
- 689 [6] S. Lee, R.M. Lueptow, Control of scale formation in reverse osmosis by membrane
690 rotation, *Desalination.* (2003). doi:10.1016/j.biortech.2012.05.044.
- 691 [7] J.Y. Park, C.K. Choi, J.J. Kim, A study on dynamic separation of silica slurry using
692 a rotating membrane filter 1. Experiments and filtrate fluxes, *Journal of Membrane*
693 *Science.* 97 (1994) 263–273. doi:10.1016/0376-7388(94)00167-W.
- 694 [8] C.A. Serra, M.R. Wiesner, A comparison of rotating and stationary membrane disk
695 filters using computational fluid dynamics, *Journal of Membrane Science.* 165 (2000)
696 19–29. doi:10.1016/S0376-7388(99)00219-7.
- 697 [9] M. Ebrahimi, O. Schmitz, S. Kerker, F. Liebermann, P. Czermak, Dynamic cross-
698 flow filtration of oilfield produced water by rotating ceramic filter discs,
699 *Desalination and Water Treatment.* 51 (2013) 1762–1768.
700 doi:10.1080/19443994.2012.694197.
- 701 [10] J. Bendick, B. Reed, P. Morrow, T. Carole, Using a high shear rotary membrane
702 system to treat shipboard wastewaters: Experimental disc diameter, rotation and flux
703 relationships, *Journal of Membrane Science.* 462 (2014) 178–184.
704 doi:10.1016/j.memsci.2014.02.015.
- 705 [11] L. Ding, M. JAFFRIN, M. Mellal, G. HE, Investigation of performances of a
706 multishaft disk (MSD) system with overlapping ceramic membranes in
707 microfiltration of mineral suspensions, *Journal of Membrane Science.* 276 (2006)
708 232–240. doi:10.1016/j.memsci.2005.09.051.
- 709 [12] S.S. Lee, A. Burt, G. Russotti, B. Buckland, Microfiltration of recombinant yeast
710 cells using a rotating disk dynamic filtration system, *Biotechnology and*
711 *Bioengineering.* 48 (1995) 386–400. doi:10.1002/bit.260480411.
- 712 [13] U. Frenander, A.S. Jönsson, Cell harvesting by cross-flow microfiltration using a
713 shear-enhanced module, *Biotechnology and Bioengineering.* 52 (1996) 397–403.
714 doi:10.1002/(SICI)1097-0290(19961105)52:3<397::AID-BIT5>3.0.CO;2-F.
- 715 [14] F. Meyer, I. Gehmlich, R. Guthke, A. Gorak, W.A. Knorre, Analysis and simulation
716 of complex interactions during dynamic microfiltration of *Escherichia coli*
717 suspensions, *Biotechnology and Bioengineering.* 59 (1998) 189–202.

- 718 doi:10.1002/(SICI)1097-0290(19980720)59:2<189::AID-BIT7>3.0.CO;2-D.
719 [15] A. Brou, L. Ding, P. Boulnois, M.Y. Jaffrin, Dynamic microfiltration of yeast
720 suspensions using rotating disks equipped with vanes, *Journal of Membrane Science*.
721 197 (2002) 269–282. doi:10.1016/S0376-7388(01)00642-1.
722 [16] W. Zhang, N. Grimi, M.Y. Jaffrin, L. Ding, Leaf protein concentration of alfalfa
723 juice by membrane technology, *Journal of Membrane Science*. 489 (2015) 183–193.
724 doi:10.1016/j.memsci.2015.03.092.
725 [17] M. Mänttari, J. Nuortila-Jokinen, M. Nyström, Influence of filtration conditions on
726 the performance of NF membranes in the filtration of paper mill total effluent,
727 *Journal of Membrane Science*. 137 (1997) 187–199. doi:10.1016/S0376-
728 7388(97)00223-8.
729 [18] R. Bott, T. Langeloh, E. Ehrfeld, Dynamic cross flow filtration, *Chemical*
730 *Engineering Journal*. 80 (2000) 245–249. doi:10.1016/S1383-5866(00)00097-6.
731 [19] K. Kim, J.-Y. Jung, J.-H. Kwon, J.-W. Yang, Dynamic microfiltration with a
732 perforated disk for effective harvesting of microalgae, *Journal of Membrane Science*.
733 475 (2015) 252–258. doi:10.1016/j.memsci.2014.10.027.
734 [20] O.A. Akoum, M.Y. Jaffrin, L. Ding, P. Paullier, C. Vanhoutte, An hydrodynamic
735 investigation of microfiltration and ultrafiltration in a vibrating membrane module,
736 *Journal of Membrane Science*. 197 (2002) 37–52. doi:10.1016/S0376-
737 7388(01)00602-0.
738 [21] J. Postlethwaite, S.R. Lamping, G.C. Leach, M.F. Hurwitz, G.J. Lye, Flux and
739 transmission characteristics of a vibrating microfiltration system operated at high
740 biomass loading, *Journal of Membrane Science*. 228 (2004) 89–101.
741 doi:10.1016/j.memsci.2003.07.025.
742 [22] A. Kola, Y. Ye, A. Ho, P. Le-Clech, V. Chen, Application of low frequency
743 transverse vibration on fouling limitation in submerged hollow fibre membranes,
744 *Journal of Membrane Science*. 409-410 (2012) 54–65.
745 doi:10.1016/j.memsci.2012.03.017.
746 [23] S. BEIER, M. GUERRA, A. GARDE, G. JONSSON, Dynamic microfiltration with
747 a vibrating hollow fiber membrane module: Filtration of yeast suspensions, *Journal*
748 *of Membrane Science*. 281 (2006) 281–287. doi:10.1016/j.memsci.2006.03.051.
749 [24] S.T. Wereley, R.M. Lueptow, Inertial particle motion in a Taylor Couette rotating
750 filter, *Phys. Fluids*. 11 (1999) 325. doi:10.1063/1.869882.
751 [25] S.T. Wereley, A. Akonur, R.M. Lueptow, Particle–fluid velocities and fouling in
752 rotating filtration of a suspension, *Journal of Membrane Science*. 209 (2002) 469–
753 484. doi:10.1016/S0376-7388(02)00365-4.
754 [26] M. Rudolph, T. Shinbrot, R.M. Lueptow, A model of mixing and transport in wavy
755 Taylor-Couette flow, *Physica D: Nonlinear Phenomena*. 121 (1998) 163–174.
756 doi:10.1016/S0167-2789(98)00149-3.
757 [27] A. Figueredo Cardero, E. Chico, L. Castilho, R. de Andrade Medronho, Particle
758 image velocimetry (PIV) study of rotating cylindrical filters for animal cell
759 perfusion processes, *Biotechnology Progress*. 28 (2012) 1491–1498.
760 doi:10.1002/btpr.1618.
761 [28] P. Francis, D.M. Martinez, F. Taghipour, B.D. Bowen, C.A. Haynes, Optimizing the
762 rotor design for controlled-shear affinity filtration using computational fluid
763 dynamics, *Biotechnology and Bioengineering*. 95 (2006) 1207–1217.

- 764 doi:10.1002/bit.21090.
- 765 [29] T. Jiang, H. Zhang, F. Yang, D. Gao, H. Du, Relationships between mechanically
766 induced hydrodynamics and membrane fouling in a novel rotating membrane
767 bioreactor, *Desalination and Water Treatment*. 51 (2013) 2850–2861.
768 doi:10.1080/19443994.2012.750794.
- 769 [30] T. Jiang, H. Zhang, H. Qiang, F. Yang, X. Xu, H. Du, Start-up of the anammox
770 process and membrane fouling analysis in a novel rotating membrane bioreactor,
771 *Desalination*. 311 (2013) 46–53. doi:10.1016/j.desal.2012.10.031.
- 772 [31] T. Li, A.W.-K. Law, M. Cetin, A.G. Fane, Fouling control of submerged hollow
773 fibre membranes by vibrations, *Journal of Membrane Science*. 427 (2013) 230–239.
774 doi:10.1016/j.memsci.2012.09.031.
- 775 [32] H. Zhang, J. Zhang, W. Jiang, F. Yang, H. Du, A new folded plate membrane
776 module for hydrodynamic characteristics improvement and flux enhancement,
777 *Separation and Purification Technology*. 154 IS - (n.d.) 36–43.
- 778 [33] L. Fillaudeau, B. Boissier, S. Ermolaev, N. Jitariouk, A. Gourdon, **Etude**
779 **hydrodynamique d'un module de filtration dynamique pour fluides alimentaires**, (2007).
- 780 [34] L. Fillaudeau, B. Boissier, A. Moreau, P. Blanpain-avet, S. Ermolaev, N. Jitariouk,
781 et al., Investigation of rotating and vibrating filtration for clarification of rough beer,
782 *Journal of Food Engineering*. 80 (2007) 206–217.
783 doi:10.1016/j.jfoodeng.2006.05.022.
- 784 [35] Y.E. Rayess, Y. Manon, N. Jitariouk, C. Albasi, M.M. Peuchot, A. Devatine, et al.,
785 Wine clarification with Rotating and Vibrating Filtration (RVF): investigation of the
786 impact of membrane material, wine composition and operating conditions, *Journal*
787 *of Membrane Science*. (2016). doi:10.1016/j.memsci.2016.03.058.
- 788 [36] T. Jiang, H. Zhang, H. Qiang, F. Yang, X. Xu, H. Du, Start-up of the anammox
789 process and membrane fouling analysis in a novel rotating membrane bioreactor,
790 *Desalination*. 311 (2013) 46–53. doi:10.1016/j.desal.2012.10.031.
- 791 [37] N. Liu, Q. Zhang, G.-L. Chin, E.-H. Ong, J. Lou, C.-W. Kang, et al., Experimental
792 investigation of hydrodynamic behavior in a real membrane bio-reactor unit, *Journal*
793 *of Membrane Science*. 353 (2010) 122–134. doi:10.1016/j.memsci.2010.02.042.
- 794 [38] X. Mao, A.J. Jaworski, Application of particle image velocimetry measurement
795 techniques to study turbulence characteristics of oscillatory flows around parallel-
796 plate structures in thermoacoustic devices, *Meas. Sci. Technol.* 21 (2010) 035403–
797 17. doi:10.1088/0957-0233/21/3/035403.
- 798 [39] B.S. Hyun, R. Balachandar, K. Yu, V.C. Patel, Assessment of PIV to measure mean
799 velocity and turbulence in open-channel flow, *Exp Fluids*. 35 (2003) 262–267.
800 doi:10.1007/s00348-003-0652-7.
- 801 [40] T. Jiang, H. Zhang, F. Yang, D. Gao, H. Du, Relationships between mechanically
802 induced hydrodynamics and membrane fouling in a novel rotating membrane
803 bioreactor, *Desalination and Water Treatment*. 51 (2013) 2850–2861.
804 doi:10.1080/19443994.2012.750794.
- 805 [41] L.O. Wilson, N.L. Schryer, Flow between a stationary and a rotating disk with
806 suction, *Journal of Fluid Mechanics*. 85 (1978) 479–496.
807 doi:10.1017/S0022112078000750.
- 808 [42] R. Bouzerar, M.Y. Jaffrin, L. Ding, P. Paullier, Influence of geometry and angular
809 velocity on performance of a rotating disk filter, *AIChE Journal*. 46 (2000) 257–265.

810
811

doi:10.1002/aic.690460206.